UNIVERSIDAD NACIONAL AUTÓNOMA DE MÉXICO

POSGRADO EN CIENCIAS E INGENIERÍA DE LA
COMPUTACIÓN

MORPHOLOGICAL ANALYSIS OF BRAIN STRUCTURES BASED ON MAGNETIC RESONANCE IMAGES (MRI)

T E S I S

QUE PARA OPTAR POR EL GRADO DE:

DOCTORA EN CIENCIAS E INGENIERÍA DE LA COMPUTACIÓN

PRESENTA:

MARIA JULIETA MATEOS OCHOA

TUTOR:
DR. ERNESTO BRIBIESCA CORREA,
INSTITUTO DE INVESTIGACIONES EN MATEMÁTICAS
APLICADAS Y EN SISTEMAS (IIMAS)

COTUTOR:
DR. JORGE A. MÁRQUEZ FLORES,
INSTITUTO DE CIENCIAS APLICADAS Y TECNOLOGÍA,

COMITÉ TUTORAL:
DR. BORIS ESCALANTE,
FACULTAD DE INGENIERÍA

México, CDMX. Diciembre 2021

UNIVERSIDAD NACIONAL AUTÓNOMA DE MÉXICO

POSGRADO EN CIENCIAS E INGIENERÍA DE LA
COMPUTACIÓN

MORPHOLOGICAL ANALYSIS OF BRAIN STRUCTURES BASED ON MAGNETIC RESONANCE IMAGES (MRI)

A DISSERTATION SUBMITTED IN PARTIAL FULFILLMENT OF THE
REQUIREMENTS FOR THE DEGREE OF
DOCTOR OF PHILOSOPHY IN THE GRADUATE PROGRAM IN COMPUTER
SCIENCE AND ENGINEERING

PRESENTS:

MARIA JULIETA MATEOS OCHOA

ADVISOR:
DR. ERNESTO BRIBIESCA CORREA,
INSTITUTO DE INVESTIGACIONES EN MATEMÁTICAS
APLICADAS Y EN SISTEMAS (IIMAS)

COADVISOR:
DR. JORGE A. MÁRQUEZ FLORES,
INSTITUTO DE CIENCIAS APLICADAS Y TECNOLOGÍA

SUPERVISORY COMMITTEE:
DR. BORIS ESCALANTE,
FACULTAD DE INGENIERÍA

México, CDMX. Diciembre 2021

I dedicate my dissertation work to my family and friends.
A special feeling of gratitude to my loving husband John, whose support during this
challenging time and words of encouragement have been essential to me.
I also dedicate this dissertation to my friends who have supported me and
made this process more enjoyable.
I feel especially grateful for my incredible children Sophia and Demian, for being there for me
throughout the entire doctorate program. Both of you have been my best cheerleaders.

Acknowledgements

Resumen

Este trabajo presenta dos métodos computacionales para estudiar la morfología de estructuras cerebrales, utilizando Imágenes de Resonancia Magnética (IRM). En la primera etapa del proyecto, se desarrolló, validó y aplicó un método basado en vóxeles para medir el ancho delos surcos cerebrales, empleando imágenes de una base de datos MIRIAD (Minimal Interval Resonance Imaging in the Alzheimer's Disease) de pacientes con Alzheimer y sujetos de control. Este método (LM basado en EDT) emplea la Transformada de Distancia Euclidiana 3D (EDT) de la superficie pial y un algoritmo de etiquetado Local Maxima (LM). El segundo método consiste en la estimación de la tortuosidad para objetos tridimensionales, utilizado el código cadena de pendiente (SCC, por susu siglas en inglés). Este método se utilizó para estimar la tortuosidad del surco central, utilizando la base de datos MIRIAD. Los resultados muestran que la pérdida de materia gris de los pacientes con Alzheimer ocasiona que los surcos se ensanchen y esto ocasiona diferencias de forma capturadas por la tortuosidad propuesta.

Abstract

This work presents two novel computational methods to study the 3D morphology of brain structures, based on Magnetic Resonance Images (MRI). In the first stage of the project a voxel-based method for measuring the sulcal width was developed, validated and applied to a database of Alzheimer's Disease (AD) patients and Control subjects. This method (EDT-based LM) employs the 3D Euclidean Distance Transform (EDT) of the pial surface and a Local Maxima (LM) labeling algorithm. The second stage consisted of estimating the tortuosity for three-dimensional objects, in particular for the central sulcus, for its anatomical relevance. When applied to the Minimal Interval Resonance Imaging in the Alzheimer's Disease (MIRIAD) database the results concurred with the hypothesis of the gray matter loss for AD patients and showed how the sulci broadened and had morphological differences captured by the proposed tortuosity.

Contents

List of Figures

List of Tables

1

Introduction

Medical imaging refers to several different technologies and processes used to create visual representations of the static and dynamic properties of the human body for diagnostic and treatment purposes. It encompasses different imaging modalities such as X-ray radiography, Fluoroscopy, Magnetic Resonance Imaging (MRI), Ultrasound, among others. Each type of technology gives different information about the area of the body being studied or treated. Because of its complexity and rapid technological advancements it has become a multidisciplinary field that requires collaboration of biologists, chemists, medical physicists, pharmacologists, computer scientists, biomedical engineers, and clinicians of all specialties.

The medical imaging diagnoses began with the discovery of the X-rays around 1895. It is characterized by being multidisciplinary. It involves the acquisition and storage of the images, as well as the registration, segmentation, computer-assisted diagnosis (CAD), and transfer systems (PACS), among others [2].

In recent years, the accelerated development of computational tools has led to significant advances in the analysis and processing of digital images, particularly medical images. This has promoted the development of new computational techniques for the reconstruction, study and interpretation of medical images [3].

In this work, the magnetic resonance imaging (MRI) technology was employed to obtain brain images; enabling the examination, measurement, and analysis of its anatomical features, in living humans. This imaging modality has particularly enriched the field of quantitative neurobiology ([4]; [5]). It also provides detailed information concerning the morphological features of various brain regions [4]. Studies of brain morphometry using

MRI are important because they have shown potential for the prognosis of neurological diseases ([6]; [7]; [8]).

Shape analysis relates to ways of statistically identifying and characterizing structural differences among populations for finding correlations between brain shape and, for example, disease severity. A large number of approaches for characterizing differences in the shape and neuroanatomical configuration of different brains have recently emerged, due to improved resolution of anatomical human brain scans and the development of new sophisticated image processing techniques. The morphometric analysis of magnetic resonance images (MRI) of the brain has become a widely used approach to investigate neuroanatomical correlations of both normal brain development and neurological disorders.

The phenomenon of magnetic resonance was discovered in the year 1946 by Felix Bloch and Edward Purcell independently. Initially, it was only used for chemical and physical analysis. It was until 1971 that Raymond Damadian proved that the times of nuclear magnetic relaxation were different for healthy tissues and for tumors, or which motivated the research and development of this technique [9]. In 1973 Paul Lauterbur showed that it was possible to create an image using MRI [10]. It was until 1977 that the first human images of MRI were acquired, and from 1983 this technique began to be used to obtain images of the brain ([11], [12],[13]). MRI has been used as support for clinical diagnosis for almost 40 years.

Currently, MRI images are the main tool for the diagnosis of various pathologies [14] thanks to the development and advances in technology. These advances range from the development of new acquisition sequences, and the use of more powerful magnets, to the implementation of new computational tools for the handling, storage, and processing of images [15].

In the present work, the interest is focused on the image processing tools for brain MRI, especially in developing new methods to quantify brain morphology. Brain morphology has become a subfield of two fields: morphometry and neuroscience. It studies the structural measures of the brain, most commonly: volume, shape, area, length, and width. These kinds of measures are usually obtained from T1 weighted MRI, as in this work. Brain morphology has been applied to identify differences in brain structures associated with a medical condition, such as Alzheimer's disease. Giovanni B. Frisoni, et al. assess the relevance of structural MRI marker in the diagnosis and treatment of

Alzheimer disease [16], Anders M. Fjell et al. present a detailed evaluation of different brain structures using the cortical volume, among other markers, to identify differences through normal aging and Alzheimer disease [17], Leah H. Somerville presents another work that uses cortical volume to understand maturity through aging [18].

A subject currently inspiring great interest is variation in cortical folding, as this relates to cognitive function [19]. The human cerebral cortex is highly folded, which provides a large surface area that fits within the skull [20]. This also comprises the most developed area of the brain, where higher brain functions such as thinking, planning, and decision making take place. The folds can also be described as a series of ridges and indentations. A brain ridge is known as a gyrus, while an indentation or depression is a sulcus or fissure [21]; approximately 70% of the cortical surface is buried in sulci [22].

1.1 | A review of the computational tools

Sulcal width has been studied as a potential biomarker for a number of diseases, particularly Alzheimer's (AD) [15; 23; 24]. Sulcal width is defined as the minimal Euclidean distance between two points on the pial surface that belongs to different sides of the sulcal basin. Only a few algorithms in the literature measure sulcal width.

The first two reports consist of object-based methods, but these generate an indirect measurement and are also highly dependent on the segmentation method [25]. Mangin [26] proposed an indirect measurement of sulcal width, dividing the total volume of cerebrospinal fluid within the sulcus by the area of a previously constructed skeletal mesh. This mesh is parallel to the sulcus walls and located at the center of the sulcus. Kochunov [6] developed the second object-based method (available in the BrainVisa software), which requires a medial mesh. This method involves tracing two vectors at each vertex to the point where they intersect with the gray matter mesh, and then the Euclidean distance is calculated between these two intersections; this process gives the average width and its standard deviation. Importantly, object-based methods produce indirect measurements of sulcal width, from which sulcal width maps cannot be constructed.

In a recent work [27], a vertex-wise method was developed for estimating the sulcal width at each point on the cortical surface. This method takes as input the pial surface

triangular mesh from the FreeSurfer software (version 5.3) and is divided into three main stages: 1) sulcal segmentation, sulcal lines, and gyral crown extraction; 2) depth map generation, referring to previous sulcal surfaces; and 3) sulcal width map estimation. The method proposed in this project provides a direct measurement that allows the estimation of the sulcal width at each point of the brain surface.

Digital representation of three-dimensional data, objects and images, has an important role in many fields, such as: computer vision, medicine, geology, anthropology, astronomy, etc. The main contribution of this kind of representation is the possibility to measure and compare different characteristics and qualities of the digitized objects [28],[29]. There is a special interest in new feature descriptors to capture and quantify the morphological characteristics of three dimensional images. For example in medical imaging, the automatic segmentation of tumors is a field of interest, in which the morphological characteristics of the tumors are valuable. Tortuosity is a morphological property that describes some aspects of the complexity of objects. Merriam-Webster dictionary defines "tortuosity" as "full of twists, turns; crooked" [30]. In this work, a method to estimate the tortuosity of 3D objects is proposed. This method allows the estimation of tortuosity in voxelized objects using the Slope Chain Code and minimizing the stair-stepping artifacts.

The tortuosity as a shape feature has been used for multiple applications, such as: measurement of tortuosity in aluminium foams using airbone ultrasound by L. H. Le et al. [31]; a fully automated tortuosity quantification system with application to corneal nerve fibers in con-focal microscopy images presented by R. Annunziata et al. [32], morphology changes of blood vessels [33].

The computation of tortuosity for 3D objects has been approached only by a few authors. Zhang and Nagy [34] presented three measures of tortuosity and their application to analyzing cracks in concrete: 1) average angle between surface normals, 2) average principal curvatures, and 3) standard deviations of principal curvatures. Their results only show that the proposed tortuosity measurements can differentiate surfaces, but did not explain which represents better the morphological changes. W. Xiao et al. [35] described the combined effect of tortuosity and surface roughness on the estimation of flow rate through a single rough joint. They analyzed how the fluid flow through rock joints is greatly influenced by the tortuosity and surface roughness. In both cases, data interpolation is necessary to obtain the corresponding meshes of the 3D objects.

This work proposes a simple measure of tortuosity for 3D voxelized objects based on the SCC approach [36], the data used to compute the SCC is directly obtained from the voxels, without the need to interpolate. It can describe and characterize a wide set of voxelized objects, such as: tumors, organs, brain structures, archaeological artifacts, and bones, among others. The main motivation is to present a simple tool to measure, quantify, and measure morphological characteristics of different three-dimensional objects.

1.2 | Thesis outline

Chapter 2 defines the most important concepts mentioned and used throughout this thesis. The sulcal with estimation method is presented and explained in chapter 3, and its application to the MIRIAD database and the results obtained. The tortuosity for three-dimensional objects is described along with its application to the Central Sulcus for the MIRIAD database in chapter 4. Finally, the conclusions and limitations of the proposed new tools are presented in chapter 5.

1.3 | Hypothesis

Brain sulci have morphological characteristics detectable in magnetic resonance images, which allow their characterization and classification between normal subjects and populations with pathologies or conditions of interest. These characteristics can be analyzed with image processing techniques and visualized with computer graphics tools.

1.4 | Aim

To develop methods to quantify morphological features of different brain structures and to evaluate the differences among populations employing MRI brain studies.

1.5 | Goals

First stage: Sulcal width computing

1. Selection of MRI studies T1-weighted for the database integration.

2. Segmentation of gray matter for each MRI study.

3. Computation of the Euclidian Distance Transform (EDT) for each gray matter volume.

4. Label of the local maxima voxels of the EDT.

5. Estimation of the sulcal width based on the local maxima voxels detected.

6. Design of computational phantoms to validate the developed method.

7. Study of the method performance variations due to the voxel anisotropy and size.

8. Computation and selection of descriptors in order to characterize each structure.

9. Application of 3D visualization and computer graphics tools for parametric images for descriptors.

10. Selecton of MRI studies database for subjects with Alzheimer's disease.

    Selection and extraction of morphological descriptors.

    Significance evaluation of the descriptors.

Second stage: Tortuosity estimation method for three-dimensional objects

1. To propose a tortuosity estimation method for 3D objects.

2. Optimization of the accuracy and resolution of the method.

3. Estimation of the tortuosity of the central sulci for the MIRIAD database.

Basic Concepts

2.1 | Brain Anatomy

The brain is a complex arrangement of near to 100 billion neurons and 10–50 trillion neuroglias, which allows humans to process, modulate, and interpret sensory stimuli; regulate the functions of the different body systems; and perform higher mental functions such as memory, imagination, and creative thought [37]. For centuries it has been studied, although in the last decades the rapid technology developments and magnetic resonance imaging (MRI) have allowed to study the brain without having to lift the skull and led to new ways to understand and analyze it.

2.1.1 | Gray matter & white matter

The nervous system has been divided into grey matter and white matter. Gray matter contains cell bodies, neuronal extensions including axons and dendrites (see Fig. 2.1), as well as synapses between extensions, glia, and blood vessels. It is primarily responsible for processing and interpreting information.

White matter is indicated due to its white appearance as a result of mainly myelinated axons, although it also contains unmyelinated axons(see Fig. 2.1). It can also include neurons when it is in close proximity to grey matter. Its job is to transmit information to other parts of the nervous system.

At a higher level, the brain is divided into three main parts: cerebrum, brainstem, and cerebellum (Fig. 2.2). For this work purposes, we are only going to define the cerebrum, its tissues and substructures.
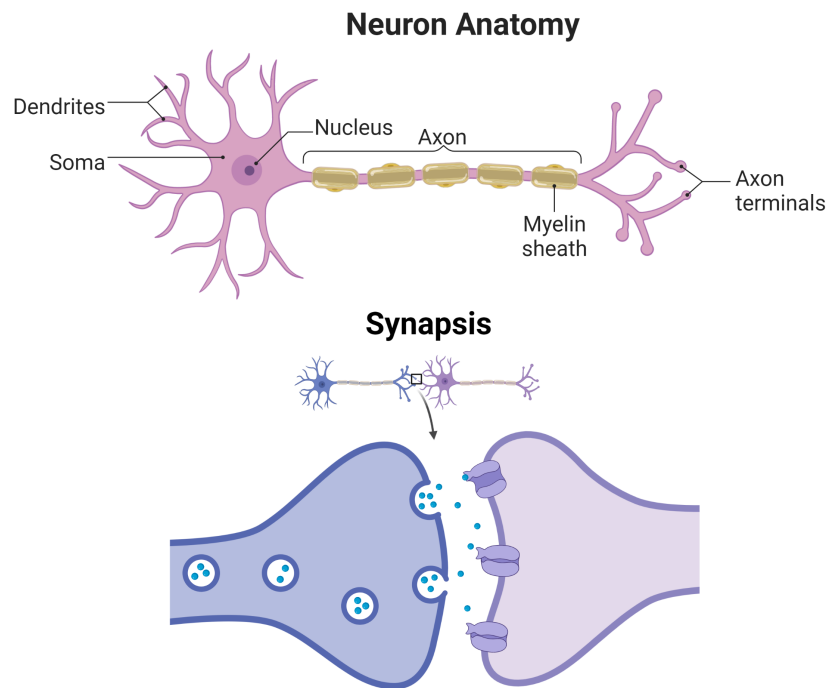
Figure 2.1: On the top, the anatomy of a neuron. On bottom, a synapses scheme. Created with BioRender.com

2.1.2 | Cerebrum

The cerebrum consists of two cerebral hemispheres that are partially connected with each other by the corpus callosum. Each hemisphere contains a cavity called the lateral ventricle, and it is responsible for different tasks. It represents one of the largest regions of the brain, and it is responsible for processing information associated with movement, smell, sensory perception, language, communication, memory, and learning. The cerebral cortex serves as the cerebrum's outer layer and is arbitrarily divided into four lobes: frontal, parietal, temporal, and occipital, as seen in Fig. 2.2.

2.1.2.1 | Cerebral cortex

The cerebral cortex has a multi-layered organizational pattern that varies through the brain. The cytoarchitecture reveals variations in cell shape, size, and density; characteristics which are used as anatomical landmarks to divide the cortex into distinct areas. The cerebral cortex is also the outer gray matter covering the cerebrum [38]. On its surface, it has bulges of brain tissue known as gyri, alternating with deep fissures known
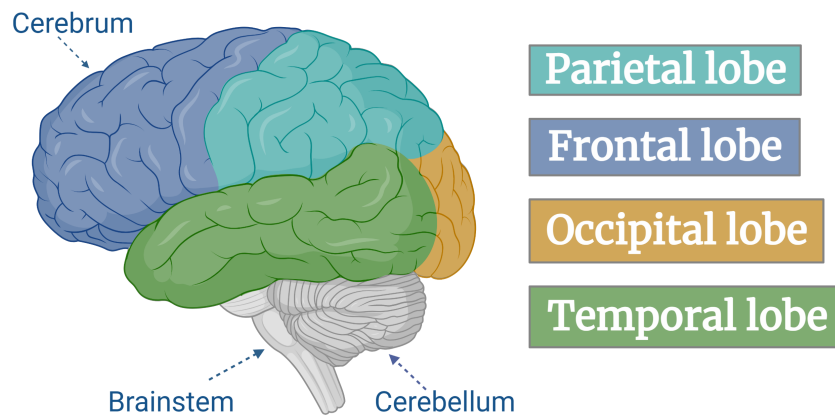
Figure 2.2: Schematic diagram of lateral aspect of left cerebral hemisphere. The three main parts are labeled; brainstem, cerebellum, and cerebrum divided in lobes. Created with BioRender.com

as sulci. The enfolding of the brain is an adaptation to brain growth during evolution. It takes place during embryonic development and is important to optimize the functional organization and wiring of the brain, as well as to allow fitting a large cortex in a limited cranial volume [39][40].

Despite variability in folding patterns among humans, there are specific types of preserved folding patterns [41]. Because of this, the shape and distribution of these patterns have been a matter of interest, as well as the possible reasons for their origin. One of the first descriptors developed to characterize these folding patterns was the degree of cortical folding (GI), this feature permits the description of a mean value for the whole brain, but also a local specific analysis of different brain regions. The GI is commonly defined as the ratio between the length of the complete contour and the length of the outer contour (without the sulci) [42]. Many other tools have been developed since then, it has represented a challenge for computational neuroanatomy, though this has significantly improved with the development of surface and voxel-based algorithms.

2.2 | Magnetic Resonance Imaging (MRI) brief description

MRI is based on nuclear magnetic resonance (NMR), whose name comes from the interaction of atomic nuclei with the imposed magnetic field when exposed to radiofrequency
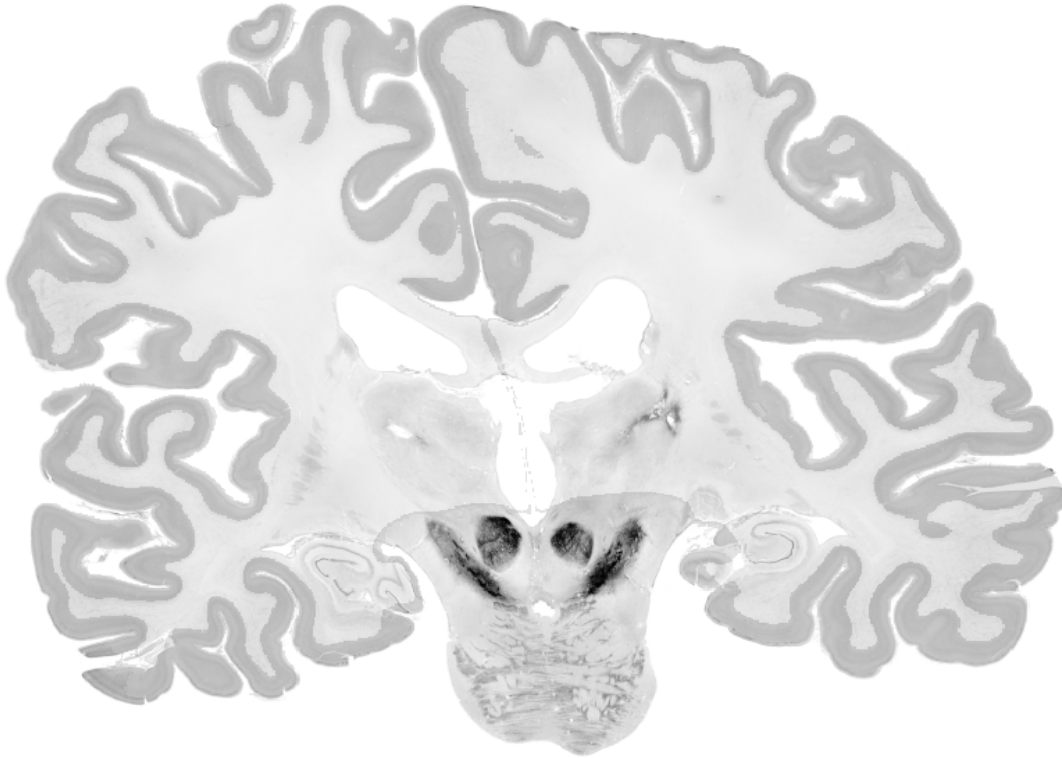
Figure 2.3: Folding patterns visible in a high resolution human brain model using the multilevel human atlas. Image obtained of the Big Brain project ($https://bigbrainproject.org/$)

(RF) electromagnetic waves of a specific resonance frequency. The first successful nuclear magnetic resonance (NMR) spectroscopy experiments were independently demonstrated in 1945 by Felix Bloch and Edward Purcell. Spatial encoding in NMR is accomplished by using magnetic field gradients, which can introduce spatial variations in the main magnetic field. Magnetic resonance imaging (MRI) was commercially used in the 1980s. It uses the same NMR signals and spatial information using tomographic sectional images of the human body in the axial coronal and sagittal planes [43].

Magnetic resonance images depend on the distribution and concentration of hydrogen nuclei in the body and on the physicochemical environment of those nuclei. It detects the magnetic moment created by single protons present hydrogen atoms. This magnetic moment aligns itself to an external field $B0$. Another possible position is alignment in the opposite direction, although this is less convenient and causes energy consumption. The energy difference between these two possible positions can be written as the quantized energy of a photon with ν being the frequency of an electromagnetic field and $\hbar$ Planck's

constant (see Eq.2.1).

$$\triangle E = \gamma \cdot \hbar \cdot B0 = \hbar \cdot \nu \qquad (2.1)$$

Hydrogen is a highly suitable element to obtain the images for its abundance in the human body, two hydrogen atoms in every water molecule [44]. The spinning protons produce small magnetic fields when a patient is placed in the MRI scanner (see Fig. 2.4, hydrogen protons align with the applied magnetic field to create a net magnetization vector. The behavior of this spin can be treated as a macroscopic magnetization M0 following the laws of classical electrodynamics. Hydrogen nuclei will provide a macroscopic magnetization when exposed to an external magnetic field, aligned in the direction of the main static field, z-direction. This rotating magnetization is called longitudinal magnetization. Applying a magnetic field perpendicular to the main static magnetic field will cause a rotation of the macroscopic magnetization. Any attempt to turn the macroscopic magnetization towards the x-y plane will cause the magnetization vector to rotate around the main direction with a frequency of 42.58 MHz/T (Larmor frequency).
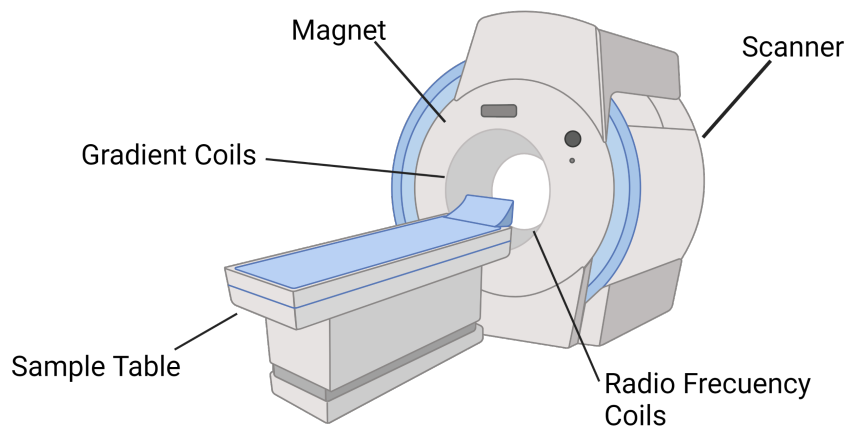
Figure 2.4: MRI scanner diagram. Created with BioRender.com

When the applied electromagnetic field uses the same frequency, one magnetic component of this field rotates with the macroscopic magnetization, generating a constant ($B1$) field. Due to this resonance situation, the magnetization can be turned around

at any angle, depending on the amplitude and duration of the $B1$ field. This process is also known as radio frequency (RF) excitation. With the $B1$ field switched off, the magnetization continues to rotate with the specific frequency of 42.58 MHz/T and will induce a signal in a nearby coil.

The amplitude of the induced signal is proportional to the number of protons involved in the excitation process. The amplitude of the induced signal depends on the actual amount of longitudinal magnetization 'flipped' into the transverse plane. The actual longitudinal magnetization is a function of the tissue-specific relaxation rate, the time needed for the realignment of the magnetization with the main magnetic field (T1-relaxation time). The rotating transverse magnetization results from of a significant number of individual magnetic moments of hydrogen nuclei, each pointing in the same direction. The dipole-dipole interaction between all these magnetic moments will cause a 'dephasing' of the transverse magnetization. The relaxation rate associated with this phenomenon is tissue-specific and is called T2-relaxation [45] [46].

2.2.1 | Brain anatomy through MRI

In the previous section, we explained in detail the MRI procedure and the information of the body we acquire from this type of images, which is a non-invasive imaging technique. Here we describe its application to the brain. The study of neuroanatomy using non-invasive imaging has allowed us to identify and characterize the different parts, sections, and structures of the brain without the need for surgery. We can also obtain some information about its function, the potential influence of the environment, the changes through development, aging, or disease. Technology developments in MRI acquisition and image processing have been essential to its application, since it provides an indirect measurement of the biological signals and anatomical information.

MRI measures radio-frequency signals emitted from hydrogen atoms after the application of electromagnetic waves and localizing the signal using spatially varying magnetic gradients. Contrast depends on the density of protons within the voxel and properties of the local tissue related to the magnetic properties of hydrogen or detected through manipulation of magnetic fields. The image contrast depends on the precise timing of the pulse sequences. In table 2.1 the different values of T1 y T2 MRI sequences for three different brain tissues are presented: Gray matter, White matter, Cerebrospinal fluid (CSF). Due to these different values, the tissues and structures are distinguishable in the images (see Fig. 2.5).

Tissue	T1(ms)	T2(ms)
Gray matter	1200	110
White matter	860	80
CSF	4500	2200

Table 2.1: Average relaxation times for different brain tissues, with a $B_0 = 3T$ [1].
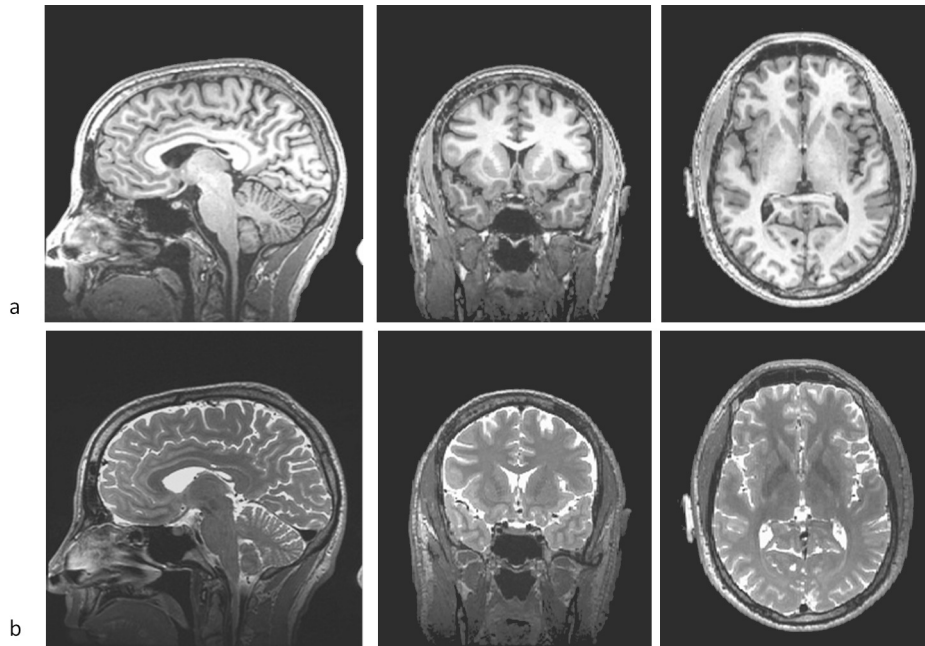
Figure 2.5: From left to right: sagittal, coronal, and horizontal planes of the brain obtained with MRI. In (a) the images were acquired with a T1-weighted sequence. The white matter has greater gray values (looks white), the gray matter appears gray, while water and CSF appear dark. Images in (b) were acquired with the T2-weighted sequence. In this type of images the white matter appears in dark gray, gray matter appears in light gray, and water and CSF appear white.

After the image acquisition, there are different approaches towards measuring and characterizing brain structures. In this thesis, we are going to take the macroscopic approach, developing new computational tools to measure shape characteristics of the brain, which considers the sizes and shapes across multiple voxels. In their work, Jason P Lerche et al. [47] proposed 5 domains to divide the macroscopic applications:

1. *Manual labeling volumes.* Trained physicians manually segment regions of interest from brain scans.

2. *Automatic segmentation algorithms*. It has allowed the individual study of each brain structure and its application to larger databases.

3. *Brain morphometry*. It aims to quantify different features of the images and the comparison among populations.

4. *Analysis of the folding pattern of the cerebral cortex*.

5. *Diffusion tractography*.

These techniques are often complementary, and it will depend on the application. For example, in this work, we analyzed some morphometric characteristics of the folding patterns and used automatic segmentation algorithms to identify the brain cortex.

The above mentioned contributions to the neuroanatomical field have changed the way we understand and analyze the brain. It has led to the development of many computational methods and imaging techniques to analyze and study brain anatomy, these together are included in emerging fields; computational neuroanatomy and quantitative imaging, among others. The main advantage of these new tools is the possibility to quantify and compare many characteristics of the brain, which has allowed us to know more about how the human brain works, and how different diseases or conditions affects it.

3

Sulcal width estimation

3.1 | Method

All the brain images analyzed in this work have been acquired by Magnetic Resonance Imaging (MRI). This work is divided in two stages:

1. The implementation of a voxel-based method to measure the sulcal width (EDT-based LM).

2. The application of the proposed method to a database with Alzheimer patients and control subjects.

3.1.1 | EDT-based LM method
First stage

A method for labeling Local Maxima based on EDT was developed to measure sulcal width. The algorithm was designed to use the discrete representation of the pial surface as input, and to compute the morphological features on a regular three-dimensional grid, comprising a voxel-based approach.

First, the pial surface EDT was computed to obtain the distance d from each voxel outside the brain, to the nearest voxel on the cortical boundary. For the purposes of this work, the unit of distance is termed Minimum Voxel Dimension (MVD) and is defined as the smallest voxel side. Equation 3.1 describes this relationship, where p is a point outside the pial surface B, and q is a point within the B boundary ∂B.

$$d(p,B) = min_{q \, \epsilon \, \partial B} \|p - q\|, p \, \epsilon \, \mathbb{R}^3 \qquad (3.1)$$

The result of this transformation is a 3D image, where the level of intensity of gray for each voxel is d. Subsequently, to work exclusively with information about sulci, this image was masked by the morphological closing (Serra, 1984) of the pial surface, with a sphere of 3 voxel radius, as the structuring element. Within each sulcus, the 3D crest lines (Local Maxima) represent half the distance between the closest borders of the sulcus. An algorithm to detect and label these Local Maxima voxels was developed. Fig. 3.1 is a two-dimensional example of the main stages in the EDT-based LM voxels algorithm.

3.1.2 | Pre-processing, segmentation pipeline

The pial surface is necessary for computing sulcal width because it represents the boundary between gray matter and cerebrospinal fluid. There are different ways of extracting it. For the purposes of this work, each structural T1-weighted MRI scan was analyzed by the FreeSurfer cross-sectional pipeline [48] in order to calculate the pial surface. The main stages in this process are pre-processing, voxel-based processing, and surface-based processing. This includes segmentation of subcortical structures, extraction of cortical surfaces, cortical thickness estimation, spatial normalization onto the FreeSurfer surface template (FsAverage), and parcellation of the cerebral cortex into units, with respect to gyral and sulcal structures. Pial surface extraction can be accomplished using any other neuroimaging software, such as Functional MRI from the brain Software Library (FSL).

3.1.3 | Pial surface EDT

After calculating the pial surface, this was converted into a binary volume, where all voxels inside the pial surface (i.e., brain tissue) were featured ("1"), and all voxels outside were not-featured ("0"). EDT computation to calculate pial volume employs the fast algorithm for three or more dimensions, designed for Matlab by [49]. This transformation provides a distance map of the pial surface; Fig. 3.1 is a 2D example of the EDT for a binary image.
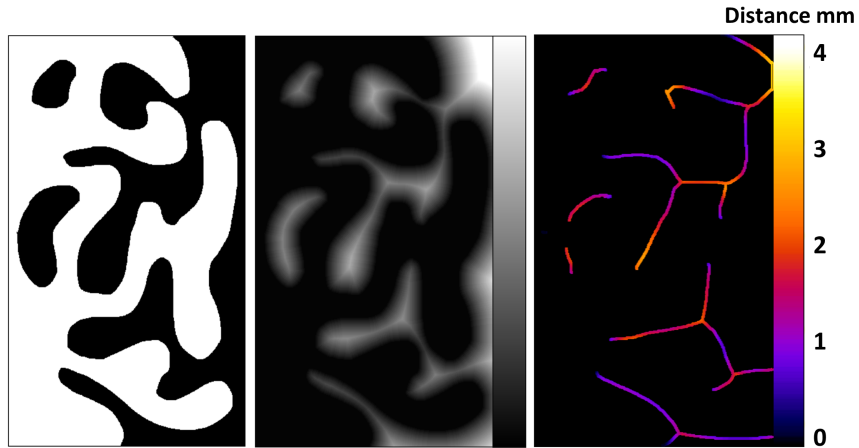
Figure 3.1: **EDT-based LM**. Left, 2D image of a simulated section of the brain cortex. Middle, EDT of the brain tissue (pial surface) of the left image. Right, LM of the EDT (middle), modulated by distance.

3.1.4 | Local Maxima labeling algorithm

A local maximum is a voxel that has the greatest intensity label within a neighborhood. The Local Maxima labeling algorithm aims to identify and label those voxels in the crest line that manifest the maximum intensity value within the search neighborhood.

Fig. 3.2 illustrates the three main components of the algorithm:

- The neighborhood to be searched, a discretized sphere (S) with radius r.

- The EDT of the object to be studied (a triangle in the case of this 2D example).

- The voxel-run intensities.

Prior to Local Maxima detection, it is necessary to define the spherical neighborhood shell S, in order to compare the voxel under examination (central voxel) with pairs of shell voxels in opposite positions N_{pairs}, for all directions. It is also necessary to define the search subvolume EDT_{vol}, employing the radius r of the chosen S and operate without exceeding the voxel-array dimensions.

The LM labeling algorithm scans the pial surface EDT_{vol} of $256 \times 256 \times 256$ voxels within the spherical search neighborhood. This scan involves reading and comparing the values of the two voxel runs made for each N_{pair} in the neighborhood shell. For
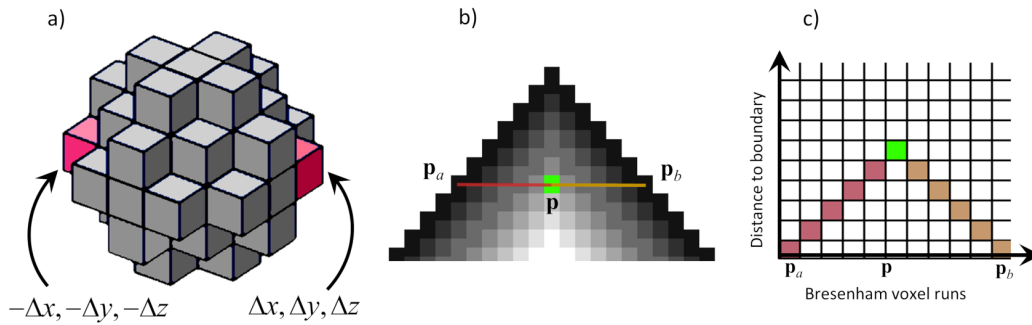
Figure 3.2: **Local Maxima Algorithm**. (a) Discrete spherical neighborhood (S) of $r = 2$; opposite offset pairs are added to test point p, resulting the pair p_a = (x-Δx, y-Δy, z -Δz), p_b= (x+Δx, y+Δy, z +Δz); (b) Inner EDT of the object; two discrete Bresenham lines, ($\overrightarrow{p_a p}$) and ($\overrightarrow{p p_b}$), are scanned for each pair in the neighborhood; (c) Bresenham voxel runs for p (green voxel). In this case, p is detected and labeled as local maximum.

the purposes of this work, the voxel runs are defined as chains of 26 connected voxels, identified, according to the Bresenham algorithm [50; 51], from the shell to the central voxel. The Bresenham algorithm determines the voxels that should be selected to trace a close approximation to a straight line between two points.

A voxel is identified as a local maximum (a Local Maxima voxel) if intensity values decrease in the S direction for both voxel runs, at least for $N_{directions}$. This means that it should follow an up-down staircase pattern (Fig. 3.2), where the highest value is the voxel being examined. The pseudo-code is presented as Algorithm3.1.4. For sulcal width computation, $r = 3$ and $N_{directions} = 7$ were selected; r was determined from the resulting mean sulcal width ($\approx$ 3 mm), and $N_{directions}$ were optimized to minimize the lack of accuracy in the algorithm.

Algorithm 1 Local Maxima Labeling Algorithm

Input:
    External pial surface EDTvol. (cols=256, rows=256 and slices=256)

Parameters:
    $N_{directions}$ Minimum number of Bresenham scan-line directions for labeling a voxel as Local Maximum.

    r Radius of the 3D neighborhood.

    count_directions A counter from 1 to $N_{direction}$

Output:
    Volume with the Local Maxima voxels labeled with half of sulcal width value.

Initialization:
    Pre-calculate the relative coordinates of the 3D neighborhood shell of radius r: $(\Delta x, \Delta y, \Delta z)$. These are signed offsets with respect to the voxel under examination $\mathbf{p} = (x, y, z)$.

    Search all different pairs of voxels in opposite positions on the shell $(N_{pairs}((\Delta x, \Delta y, \Delta z), (-\Delta x, -\Delta y, -\Delta z)))$.

    Calculate, for each $\mathbf{p}$: $\mathbf{p}_a = (x-\Delta x, y-\Delta y, z-\Delta z)$ and $\mathbf{p}_b = (x+\Delta x, y+\Delta y, z+\Delta z)$

    Let $[\mathbf{p}_a, \mathbf{p}]$ and $[\mathbf{p}_b, \mathbf{p}]$ be the intervals of points defined by the Bresenham lines $\overrightarrow{\mathbf{p_a p}}$ and $\overrightarrow{\mathbf{p p_b}}$, respectively.

    Note that $Ndirections < Npairs$.

    Define the search subvolume as $EDTvol$ as $[r, cols-r-1] \times [r, rows-r-1] \times [r, slices-r-1]$.

Core steps:
1. **for all p $\in$ *EDTvol* do**
2.   **for all** N_{pairs} **do**
3.   *count_directions*=1
4.   **for all $\mathbf{p}_k \in [\mathbf{p}_a, \mathbf{p}]$ AND $\mathbf{q}_k \in [\mathbf{p}_b, \mathbf{p}]$ do**
5.   *count_directions* = *count_directions*+1
6.   **if** *count_directions* = *Ndirections*
                then break
7.   **if** $EDT(\mathbf{p}_k) < EDT(\mathbf{p}_{k+1})$ **AND** $EDT(\mathbf{q}_k) < EDT(\mathbf{q}_{k+1})$
              then $V_{out}(\mathbf{p}) = EDT(\mathbf{p})$ # p is a Local Maximum
            end if
        end for
        end for
    end for

To obtain the sulcal width at each Local Maximum, the corresponding value of the EDT_{vol} is multiplied by two because the maximum is located at half the distance between the closest opposing pial voxels, i.e. half the sulcal width at these voxels. The mea-

surements obtained from the EDT-based LM vary in terms of depth and along the sulci, suggesting morphology changes inside the sulci. This detailed information is of great interest and can be summarized by computing morphological descriptors for each sulcus. To compare these measurements among patients, with the application implemented here, each sulcus was identified based on the Destrieux atlas [52], and summarizing values were computed, i.e., the MSW and the MAD for the width values within the sulcus.

3.2 | Results

3.2.1 | EDT-based LM

This section presents the results of the method validation, and its application to the MIRAD database.

3.2.1.1 | Validation

To model width variations within 3D objects and test the performance of the developed method, an helicoidal horn phantom was designed (see A), exhibiting variations in parameters, for example 3D orientation, radii (width), and non-planarity, as shown in Fig. 3.3a. The phantom's main characteristics are the angle shifts and radius (R_{horn}) variations. The R_{horn} value for every θ angle is known as is the position of the crest line (Fig. 3.3b). The crest line voxels follow $R_{horn} < \epsilon$ for each θ (ϵ was set as 1 MVD), in contrast with the theoretical approach in which the crest line voxels comply with R_{horn} = 0. The results of the EDT-based LM method, applied to the helicoidal horn for seven directions, are illustrated in Fig. 3.3c and were compared with the phantom information.

The identification of the Local Maxima voxels is affected by image resolution and discretization artifacts. These can make those voxels outside the crest line comply with the criterion in at least one direction (Fig. 3.4, two and five directions), causing them to be mislabeled; thus, increasing the inaccuracy (δ) of the method. Voxels in the crest line match this criterion in the case of most directions, but for small R_{horn} values, this number of directions decreases, creating holes (Fig. 3.4, seven and ten directions). The number of directions was optimized to minimize inaccuracy and maximize the labeling of voxels in the crest line. To quantify inaccuracy, R_{horn} theoretical values were compared with
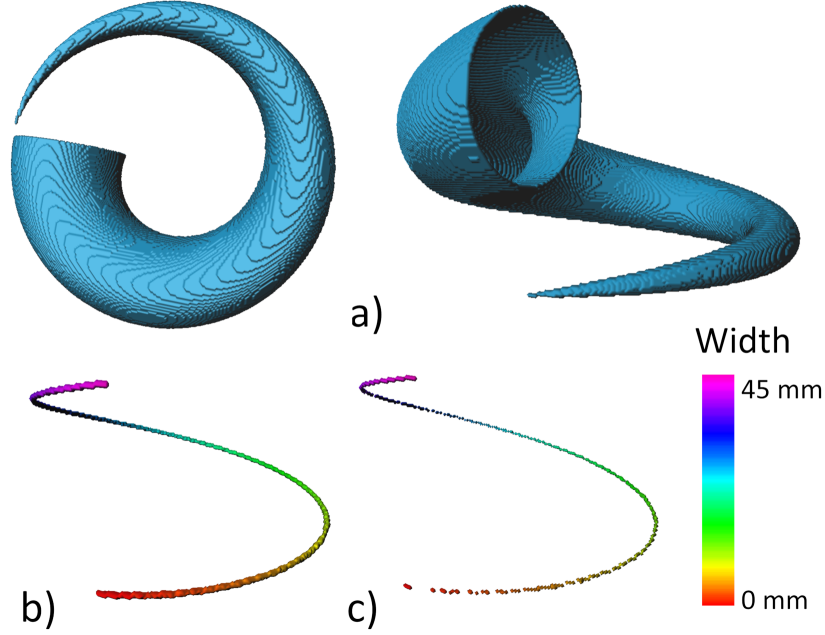
Figure 3.3: **Computational phantom design**. a) Discrete helicoidal horn with R_{horn} (θ). b) Discrete helicoidal horn with R_{horn} $(\theta) < \epsilon$. c) EDT-based LM algorithm result based on a seven-direction criterion.

those obtained using the proposed method.

After considering both factors: 1) mislabeling of Local Maxima voxels, and 2) discretization errors, the following equation is proposed:

$$\delta = D' - (D - d) \tag{3.2}$$

D' D' is the output of the EDT-based LM multiplied by two.

D D is theoretically the shortest distance from the local maximum labeled voxel to the phantom boundary.

d d is theoretically the shortest distance from the local maximum, labeled voxel to the helicoidal horn axis of the phantom. Note that ideally $d = 0$.

δ computation was made for $N_{directions} \in [2,10]$ to determine which value maximizes accuracy and to guarantee that voxels labeled as local maximum pertain to the crest line. Evidently, the value of $N_{directions}$ that maximizes the accuracy of the method is 7, and the sulcal width varies between 1 and 7 MVD, with $\delta \in [0.01, 0.45]$ MVD (Fig. 3.4).

A detailed analysis was made to define the conditions of method applicability: voxel size and voxel anisotropy. A triangular prism-shaped phantom was built (Fig. 3.5a),
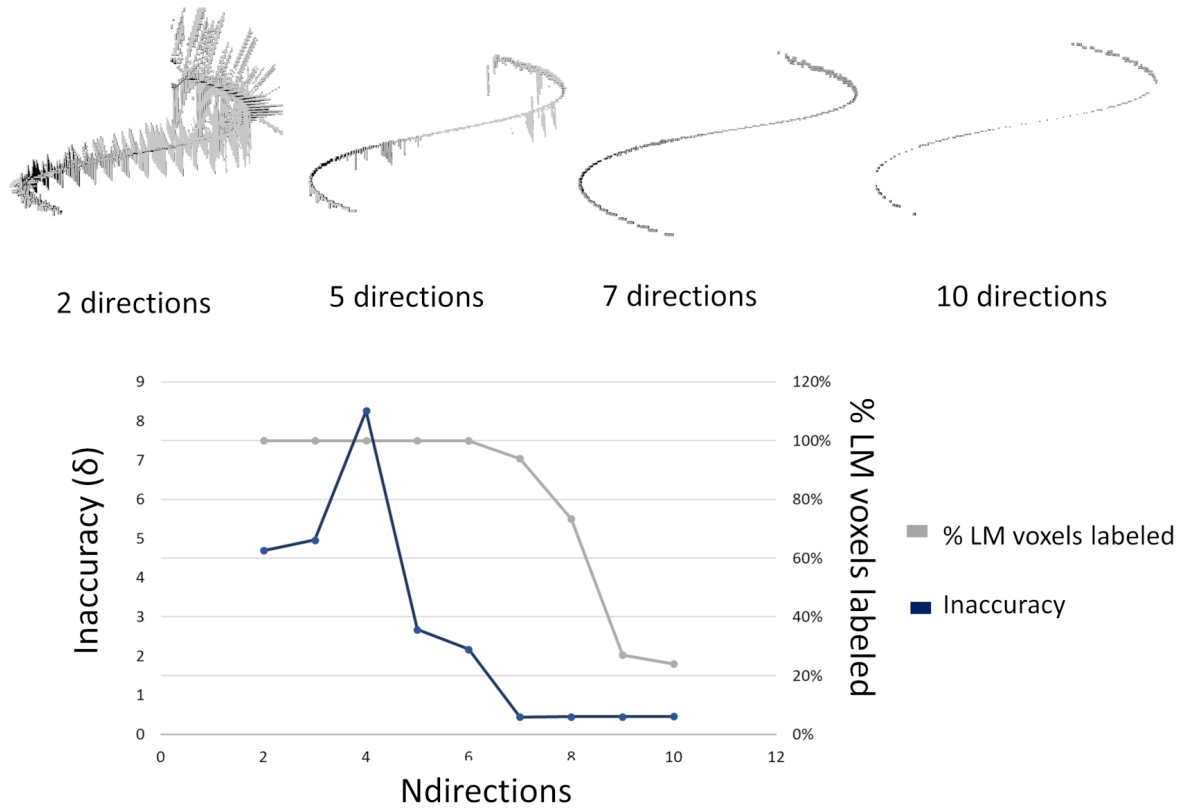
Figure 3.4: $N_{directions}$ **optimization**. At the top, helicoidal horn EDT-based LM results for 2, 5, 7 and 10 directions (from left to right). At the bottom, δ values (blue line) and rate of crest line voxels labeled (gray line) for directions between 2 and 10. Voxels with label >0 are shown in gray.

making a full angular evaluation possible. Fig. 3.5 shows the triangular prism shaped-phantom, a voxel-based representation along with its construction parameters.

For the angular evaluation the phantom parameters were selected as follows: length=100 mm, height=50 mm, width=20 mm, and orientation angles: θ (around Z axis) =0°, Φ (around Y axis)=0°,, and Ψ(around X axis) ϵ [0°, 90°,], Ψ is also known as the pitch. For the purposes of this work, a $256 \times 256 \times 256$ mm^{3}array was employed.

A voxel size evaluation was performed to determine the maximum value for accurately measured widths, ranging between 1 and 6 mm. The method was applied to the triangular prism-shaped phantom, using different voxel sizes. Mean width, percentage of Local Maxima voxels, and their inaccuracy were obtained for each voxel size and Ψ value; results are presented in Fig. 3.5. In the graph on the left, the y-axis represents the
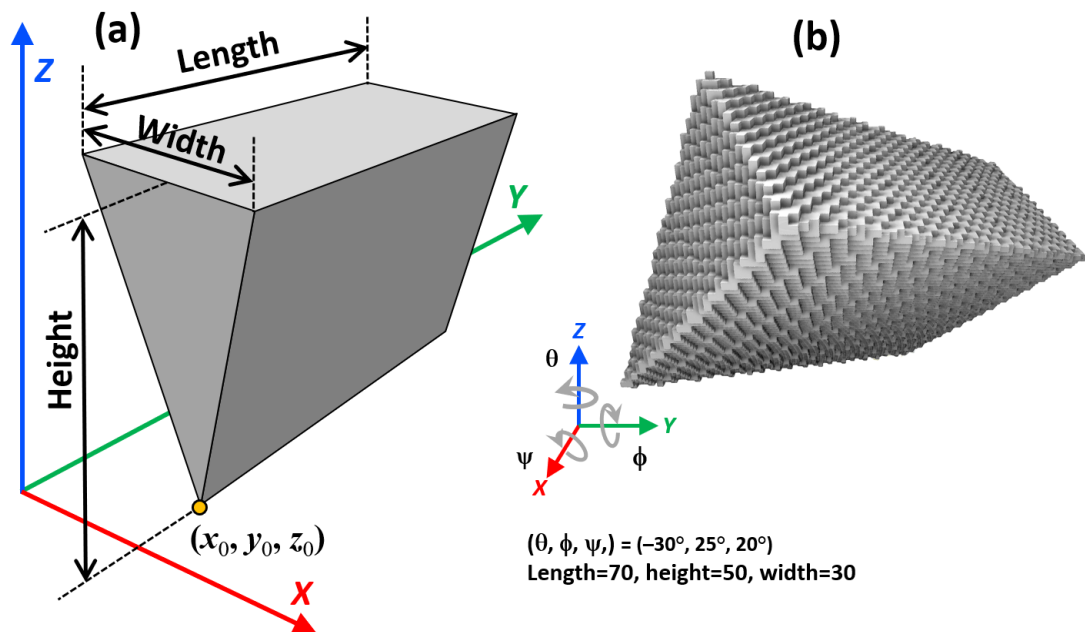
Figure 3.5: **Triangular prism** (a) Diagram of a triangular prism and its parameters. (b) Voxel-based representation of the triangular prism-shaped phantom.

Ψ values, in which the phantom is generated, the x-axis represents the different isotropic voxel sizes tested, and the colors represent inaccuracy (mm). In the graph on the right, the y-axis represents the Ψ values, the x-axis represents the different isotropic voxel sizes tested and the colors are the percentage of Local Maxima detected, respectively. The percentage of Local Maxima voxels is computed, based on results obtained for a voxel size of $1 \times 1 \times 1$ mm.
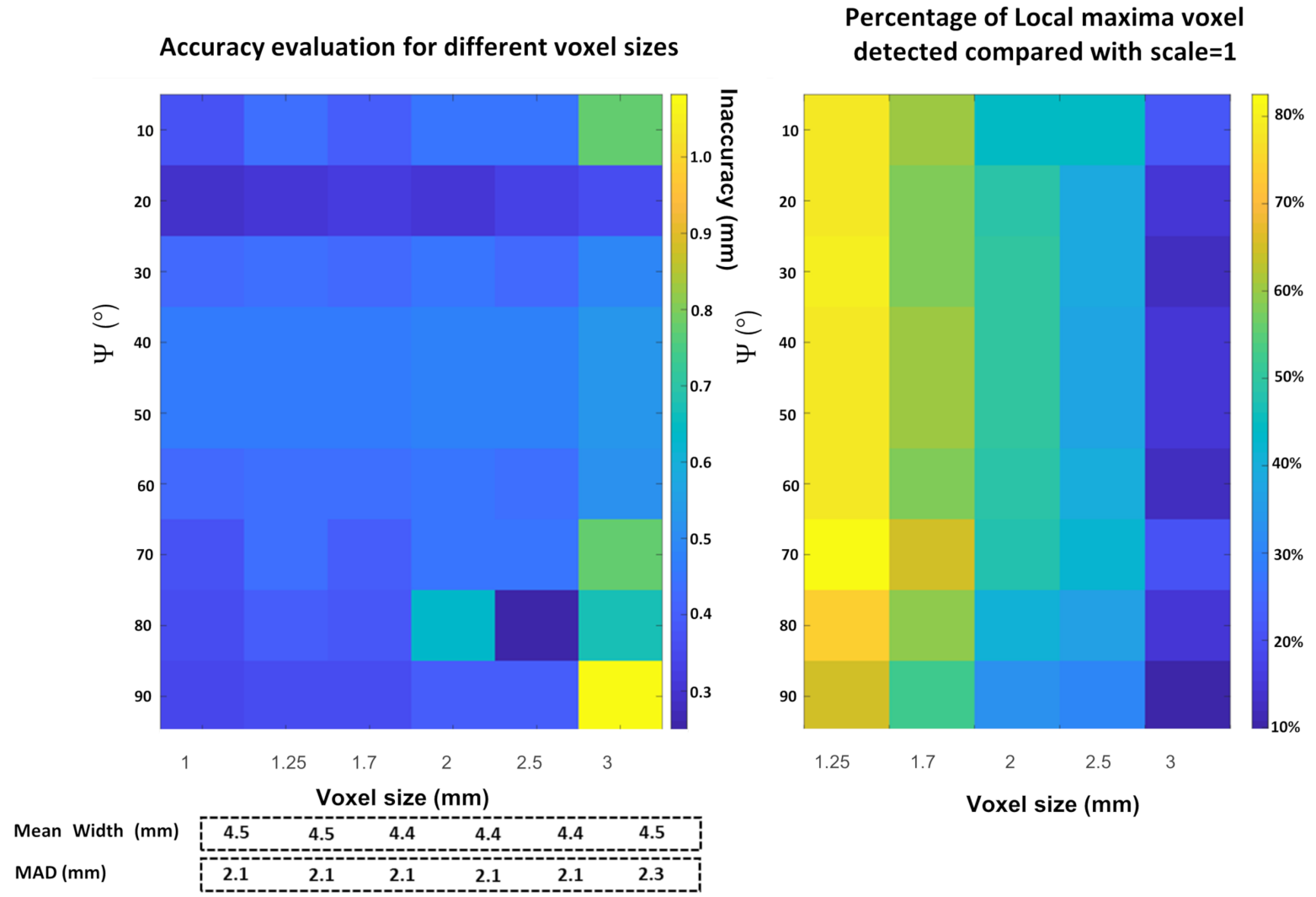
Figure 3.6: **Accuracy evaluation for different voxel size**. Left, variation in average accuracy, with size and orientation. Right, variation in the percentage of Local Maxima voxels detected (compared to those obtained for a $1 \times 1 \times 1$ mm size) for different sizes of isotropic voxels and Ψ values.

Accuracy evaluation for anisotropic voxels
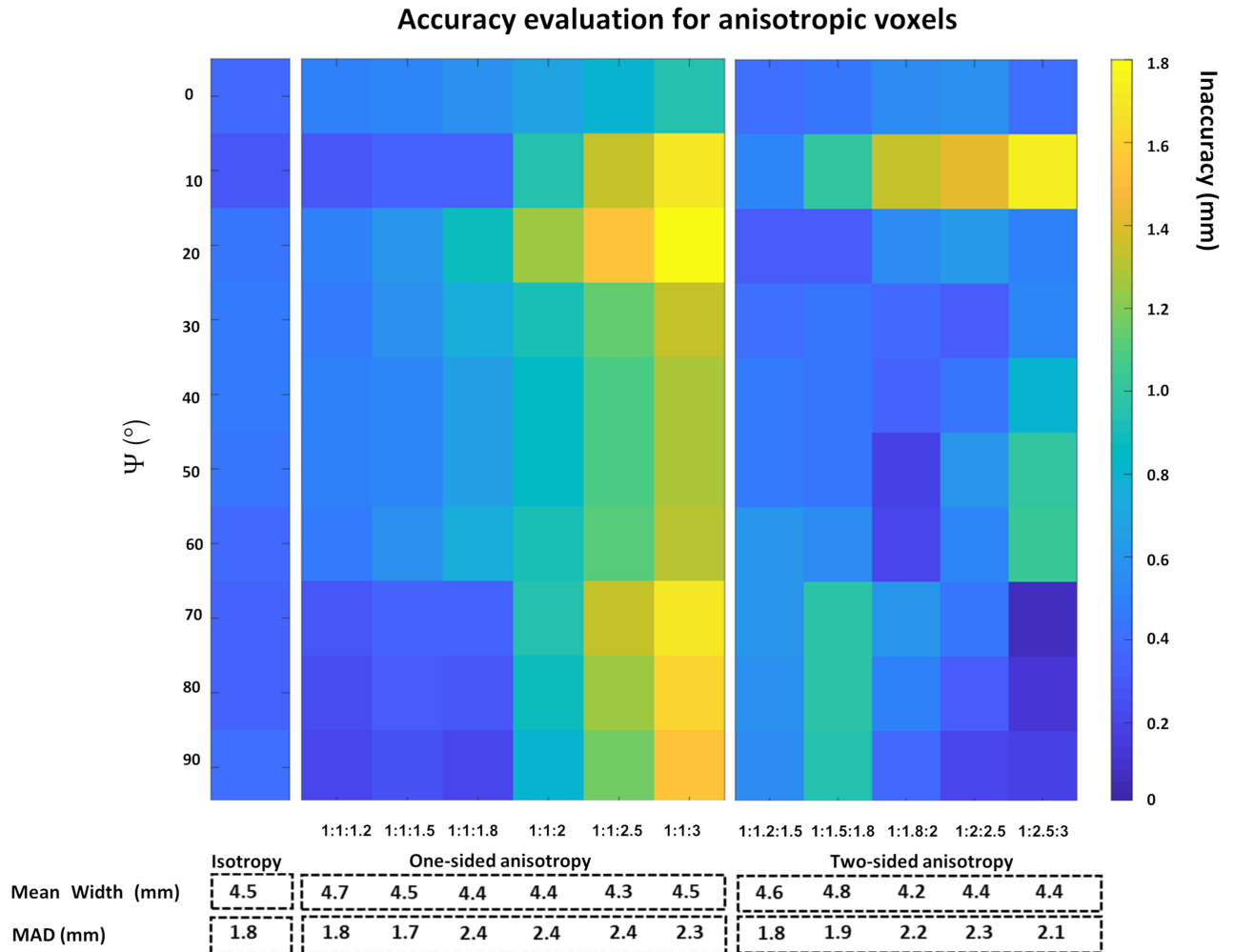
Figure 3.7: **Accuracy evaluation for different voxel anisotropy**.Left, accuracy evaluation for isotropic voxels from different orientations. Middle, accuracy variations for different values of one-sided anisotropy and orientations. Right, accuracy variations for different cases of two-sided anisotropy and orientations.

The maximum voxel size for which the application of the EDT-based LM method is recommended for measuring widths between 1 and 6 mm, is 2.5 mm for each voxel side. Fig. 3.6 shows how inaccuracy increases when voxel size reaches 3 mm per side or larger; likewise, the percentage of Local Maxima voxels detected decreases significantly, due to discretization errors.

Anisotropy robustness was evaluated in a way similar to the voxel size accuracy, pre-

viously described. Fig. 3.7 presents the results from this analysis; in each case, accuracy variation was measured for each Ψ angle. On the left, the isotropic case is presented as reference, with values of $\delta \, \epsilon \, [0, 0.45]$ mm. These are consistent with results obtained using the helicoidal horn. In the middle, an evaluation for different values of one-sided anisotropy was made; in this case one side is different from the others. On the right, the results for the two-sided anisotropy analysis are presented; in this case all the voxel sides are different.

The developed method can be used with different voxel sizes and different anisotropy conditions. Based on the accuracy values obtained, the applicability conditions recommended are: 1) for one-sided anisotropy, a limit of 1:1:1.5 aspect ratio, 2) for two-sided anisotropy, a maximum aspect ratio of 1:1.2:1.5, and 3) a maximum voxel size of 2.5 mm.
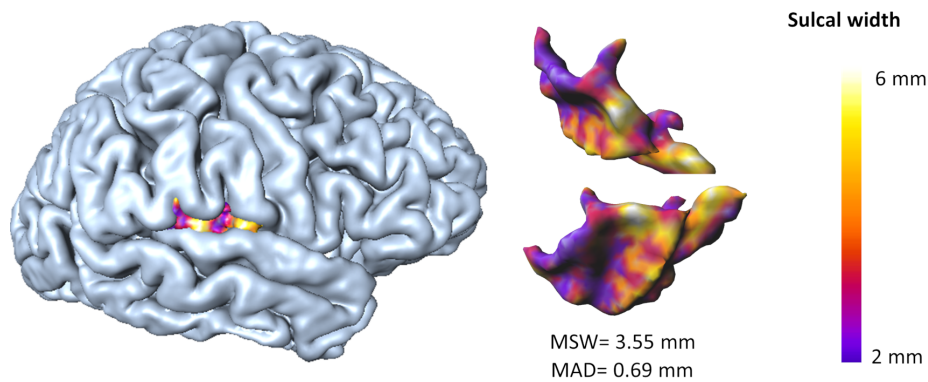
Figure 3.8: **Sulcal width of the right transverse temporal sulcus.**

3.2.2 | Application to brain images

The goal of this section is to apply the developed method to brain MRI studies, and evaluate its capability to differentiate between a group of patients with AD and a group of matched controls. The decision to test the method using this dataset was made because AD causes a significant loss of gray matter ([53]; [54]; [55]); some sulci are thus expected to broaden ([23]).

Measurements for all sulcal regions were obtained with a T1-weighted brain MRI from a single subject. The sulcal regions were identified by subtracting the brain closing volume and the pial surface. Subsequently, the anatomical labeling of the sulci was undertaken, based on the Destrieux cortical atlas [52]. For each sulcus, an estimation of MSW and MAD descriptors, was performed. Fig. 3.8 shows the sulcal width map for the transverse temporal sulcus of the right hemisphere. Changes in sulcal width are detected for this sulcus; the measurements obtained were between 2 and 7 mm, with an MSW of 3.55 mm and a MAD of 0.69 mm. Applying the EDT-based LM method to the brain endorses a depth and length-based analysis of sulcal width, which can be used to evaluate variations, spatial relations and morphology trends.

The dataset, obtained from the MIRIAD [56], includes MRI scans taken from 66 subjects on the same 1.5 Tesla Signa MRI scanner (GE Medical systems, Milwaukee, WI). The database is publicly available at Minimal Interval Resonance Imaging in Alzheimer's Diseases site (MIRIAD).

Three-dimensional T1-weighted brain images were acquired from a FOV (field of view) of $240 \times 240 \times 186$ mm, in a $256 \times 256 \times 256$ matrix, resulting in a voxel size of $0.94 \times 0.94 \times 1.5$ mm^3. All MRI images were processed, employing the FreeSurfer cross-sectional pipeline, and the EDT-based LM was to further estimate the MSW and MAD for each sulcus and compared between groups by applying a Wilcoxon rank-sum test. Significance was defined as p < 0.05 and corrected for multiple comparisons (80 sulci), with a false discovery rate of 0.05.

Fig. 3.9 shows the application of the proposed method to the MIRIAD database. a) Sulcal width map for a control subject. b) Sulcal width map for a patient. Anatomical differences between these two subjects are visually evident; the sulci of the patient's brain are wider, and the results of the EDT-based LM method are consistent with these differences. These sulcal width maps portray the fact that the variations of the average Sulcal Width for each sulcus ($\overline{SW}$) are different among brain regions.
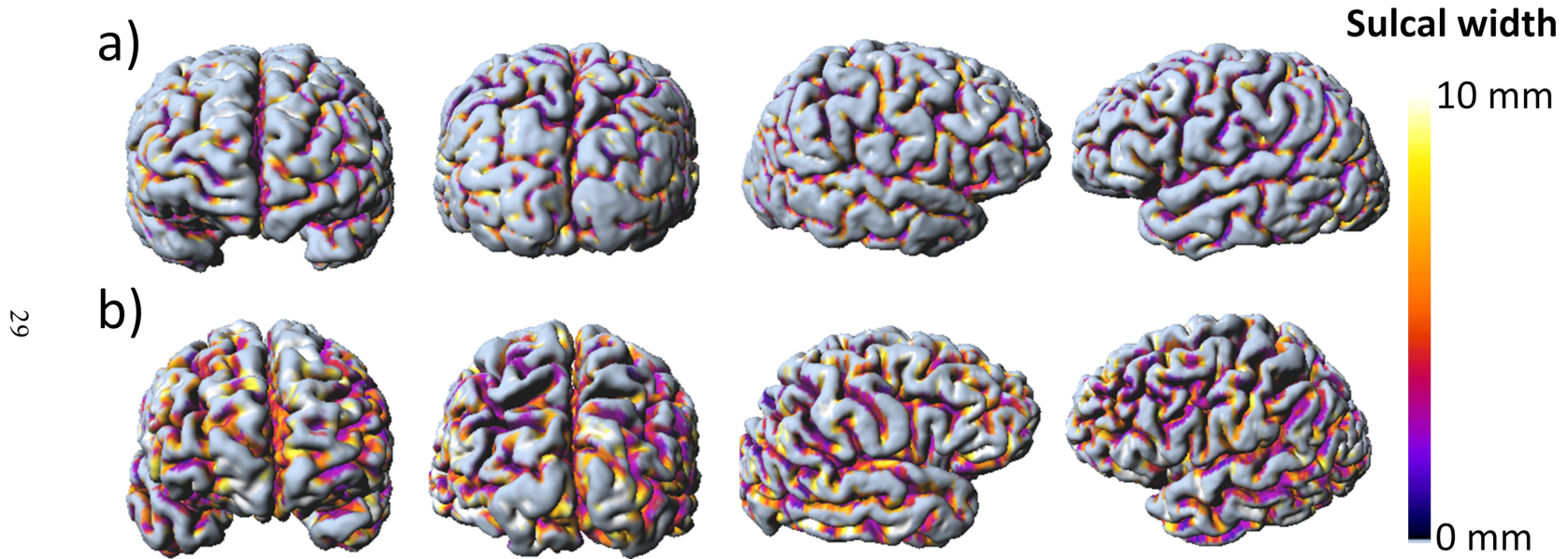
Figure 3.9: **Sulcal width measurements computed by applying the EDT-based LM method**. Frontal, posterior and lateral brain views from (a) Control Subject and (b) AD patient
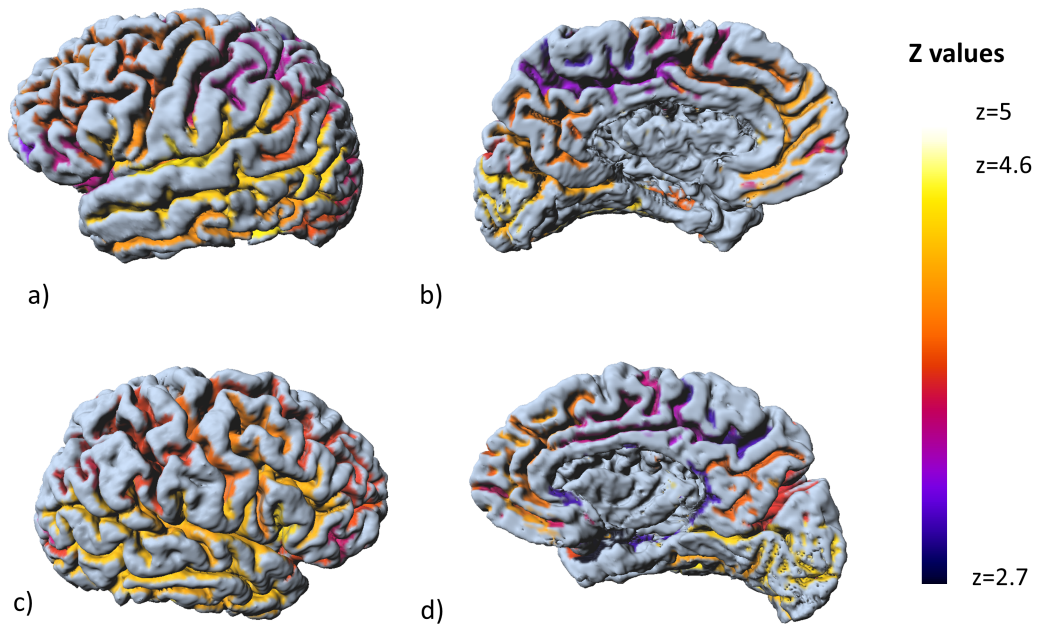
Figure 3.10: **Differences in sulcal width** between 43 patients with mild-moderate Alzheimer's disease and 23 controls (z values, Wilcoxon Rank Sum Test; p <0.05, False Discovery Rate (FDR) corrected). a) Lateral view of the left hemisphere, b) medial view of the left hemisphere, c) lateral view of the right hemisphere, d) medial view of the right hemisphere.

For the 80 sulci tested, MSW increased significantly among the patients, compared to controls. Fig. 3.10 shows the z values for these sulci. The sulci with greatest differences in MSW (higher z values) are located in the frontal and temporal lobes.

In their research, Im, Kiho et al. discovered that the greatest sulcal widening in the AD group was in the temporal lobe, concurring with our results. Liu et al. measured the sulcal width of five different sulci (Sylvian fissure, central, intra-parietal, superior frontal and superior temporal sulci) and made a comparison between control, very mild AD and mild AD, and only the intra-parietal sulcus width showed no differences [57]. The results showed significant differences for these five sulci. This is consistent with the finding of sulcal widening in the frontal and temporal lobes [55].

In the case of MAD, which measures sulcal width variability, 12 sulci showed significant differences between groups. Fig. 3.11 shows the z values mapped on the brain for these sulci.
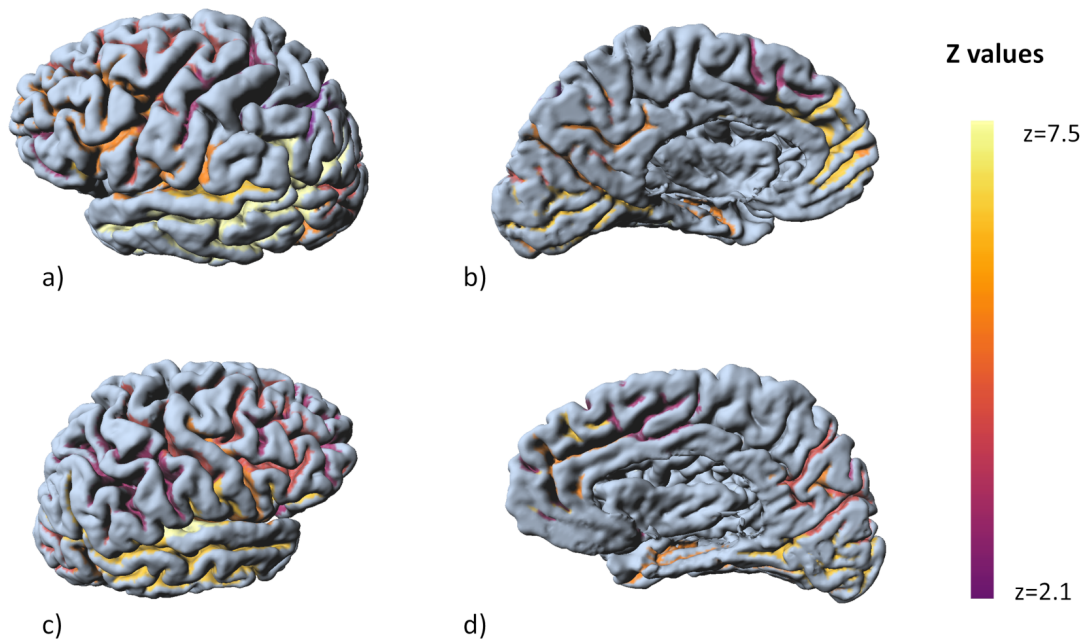
Figure 3.11: **Differences in the sulcal morphology variation** between 42 patients with mild-moderate Alzheimer's disease and 23 controls (z values, Wilcoxon Rank Sum Test; $p <0.05$, FDR corrected). a) Lateral view of the left hemisphere, b) medial view from the left hemisphere, c) lateral view of the right hemisphere, d) medial view from the right hemisphere.

Sulci results with statistical significance in terms of MAD measurements are located at the temporal and frontal lobes. This result complies with MSW results. In AD patients, sulcal width variability is lower in the frontal lobe and higher in the temporal lobe.

Finally, a Spearman correlation was performed between the Mini-Mental State Examination (MMSE) scores and both descriptors (MSW and MAD) to determine whether sulcal width was related to the MMSE score in the AD group. For both descriptors, some sulci had p values lower than 0.05; however, none of these survived the correction for multiple comparisons. The correlation coefficient value for all correlations is negative, meaning that if sulcal width or variability in sulcal width increases, the MMSE score (i.e., cognitive performance) decreases.

In the work of [23], the authors measure the mean sulcal span and compare it with the MMSE scores, which show similar results, i.e., negative correlations for all sulci

([23]).

3.3 | Discussion

The EDT-based LM method is able to identify and label most of the Local Maxima voxels and measure the sulcal width value for each of the labeled voxels. All parameters were optimized to maximize the number of crest line voxels labeled and minimize inaccuracy; this was accomplished using the designed helicoidal horn computational phantom. This method is limited by the EDT resolution and the discretization artifacts. To determine the range of voxel size and voxel anisotropy to use this method a triangular-prism shaped phantom was designed and employed. For the different voxel sizes analyzed, the MSW and MAD do not vary significantly because the increase in voxel size mostly affects the number of Local Maxima voxels detected, even though the inaccuracy of the method increases with voxel size. In the case of anisotropy, the analysis was performed for two anisotropy cases; one-sided anisotropy, in which only one side is different, and a two-sided anisotropy, in which the three voxel sides are different.

The results for the one-sided anisotropy (Fig. 3.7, middle) show that the MSW and MAD do not change significantly, but the inaccuracy values increase with the one-sided anisotropy. In the case of two-sided anisotropy, results are similar (Fig. 3.7, right), the MSW and MAD do not change significantly, and the inaccuracy values increase as two-sided anisotropy increases. The highest values of inaccuracy are obtained for $\Psi = 10^o$ as a result of the discretization artifacts of the computational phantom. The conditions of use for the EDT-based LM method are: 1) for anisotropy, a limit of 1:1:1.5 aspect ratio, 2) for two-sided anisotropy, a maximum aspect ratio of 1:1.2:1.5, and 3) a maximum voxel size of 2.5 mm. After the validation process, it was concluded that the developed method is sensitive to the variability of the sulcal morphology, throughout the brain.

The Destrieux atlas to obtain the cortex labels was chosen because it divided the cortex into gyral and sulcal regions, facilitating the labeling of most sulci. An algorithm was developed to use these cortex labels to fill the corresponding sulcal volume; which facilitates the identification, analysis of individual sulcal width values and their subsequent comparison. One of the main advantages of the EDT-based LM method, compared to the object-based methods previously described, is that sulcal width maps can be computed; these maps reveal any morphological changes either within a single sulcus or involving the entire brain sulcal region, but only enable a qualitative examination.

Even though the proposed method is not voxel-wise, sulcal width variation can be analyzed and characterized by morphological descriptors. The sensibility of the proposed method, to detect sulcal width differences between a control group and a mild AD group, was evaluated, measuring two morphological descriptors MSW and MAD. Evidently, MSW values were significantly higher for the eighty labeled sulci, in patients with AD. These results suggest that gray matter loss associated with AD ([55]) is closely related to the increase in sulcal width, which is more evident in the frontal and temporal lobes. The variability in sulcal width (MAD) only changed significantly in the case of eight sulci. This lack of significant differences between control and AD patients, in terms of the MAD values for most sulci, suggest that they broaden globally. The relationship between sulcal width and cognitive function, via the MMSE score, was analyzed, even though these results did not survive the correction for multiple comparisons. However, some results suggest the possibility of a significant relationship, if a larger sample is used. Further research is necessary to explore the value of this detailed information, as a marker of disease progression.

MSW measurements were also obtained; using the object-based method (BrainVisa) for the sixty-six subjects, to compare data obtained using each method, and determine the degree of correlation between them. The Brain Visa atlas was also used to label the sulci and compute sulcal width, employing the EDT-based LM method. The detailed comparison was made for five from each hemisphere, the MSW values were poorly correlated between both methods and only for the central sulcus correlation coefficient was r >0.5. This case can be explained because of the well-defined morphology of this sulcus. The general lack of correlation between these two methods may relate to differences in approach; the Object Based sulcal width is computed, applying the distance between vertexes and using the EDT-based LM method, sulcal width represents the distance between voxels, this comparison was made with the Brain Visa Atlas which label 125 sulci. The main shortcoming for this method is that the labeling algorithm misses some of the Local Maxima voxels, which makes it impossible to be voxel-wise as is.

3.4 | Comparison with BrainVisa

The sulcal width measurements obtained using the EDT-based LM method were compared, to those obtained using the object based morphometry method ([6]), which is available as a BrainVisa tool. For this purpose, all the images of the MIRIAD database were labeled with the BrainVisa altlas, then, the mean sulcal width of four sulci (Central, Temporal Superior, Superior Frontal and Inferior Frontal) was computed, using both methods. These measurements were obtained for each subject and both hemispheres.

A correlation analysis was performed to determine how the EDT-based LM sulcal width measurements, for an individual sulcus, are related to those obtained using the object-based method for the same sulci. The $(\overline{SW})$ and the standard deviation for all subjects of the MIRIAD database were obtained for each individual sulcus using both methods, and likewise the correlation coefficient (r) was computed for each sulcus. The sulcus presenting the biggest differences between methods is the Superior Frontal sulcus for both hemispheres.

The highest values for the correlation coefficient (r ϵ [0.39 0.68]) are obtained for the Central and Temporal Superior sulci. r values close to one mean stronger linear correlation. For the Superior Frontal and the Inferior Frontal sulci, the r ϵ [0.12 0.39]. In Fig. 3.12, the relationship between the measurements using the two different methods can be appreciated more clearly; at the top, the sulci measurements with higher correlation values for both hemispheres are displayed; at the bottom, the sulci measurements with lower correlation values are displayed; even if the correlation is not strong, both have similar tendencies.
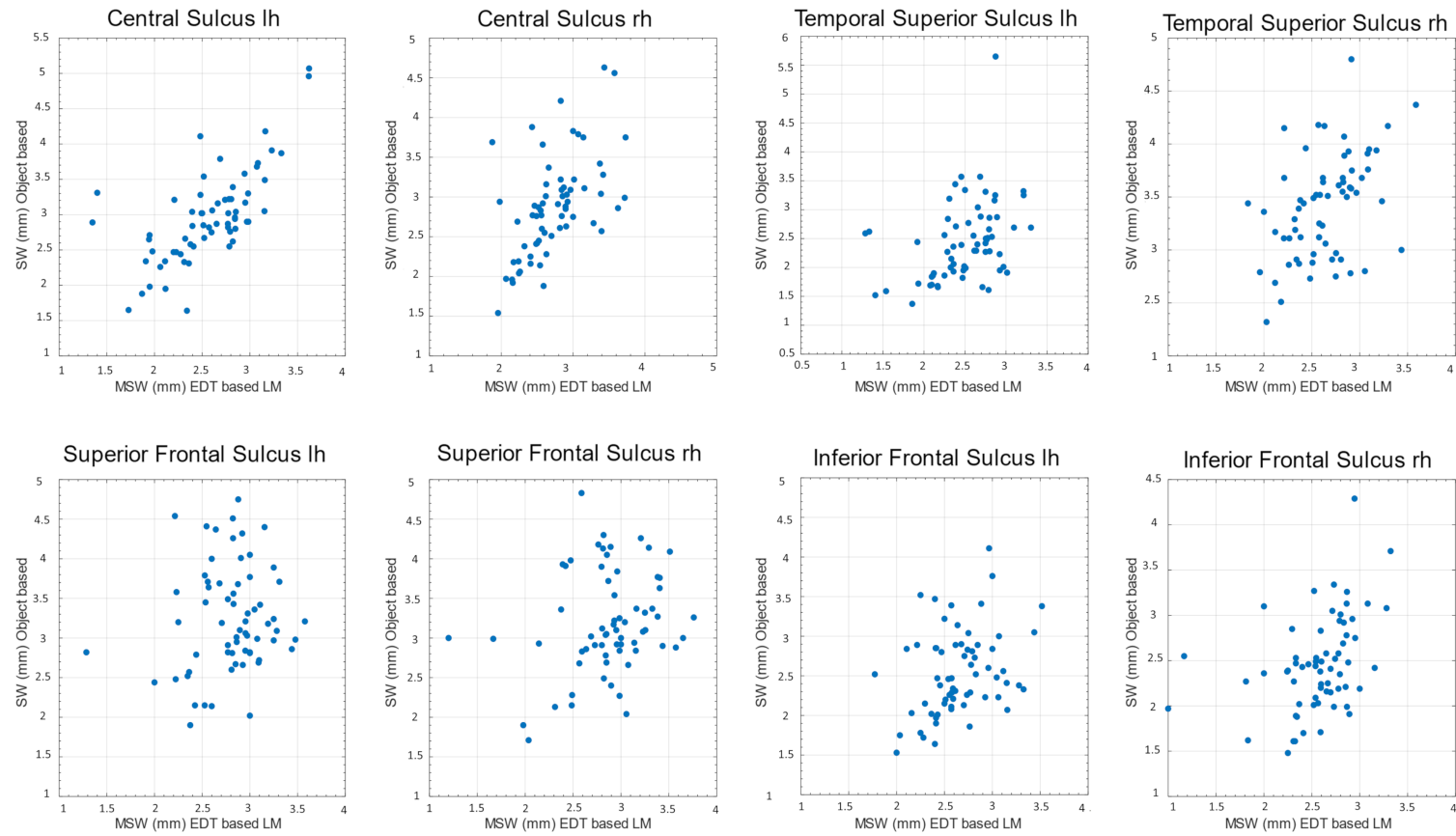
Figure 3.12: **Comparison between methods**. Relationship between the sulcal width measurements computed using both methods: EDT-based LM (x-axis), and Object based (y-axis).

Tortuosity estimation for three-dimensional objects

The classical, simple, and most widely used definition to measure vessel tortuosity [58] is the ratio between the arc length of the curve (C) and the length of the underlying chord (L), which is the line segment joining two points, $\tau = C/L$. A drawback of this approach is its failure to compute tortuosity correctly. In Fig. 4.1 two curves with different shapes, both preserving the same length of the curve and underlying chord are presented, Curve a has significantly more turns and twists, and therefore it is more tortuous than curve b, but according to this definition $\tau_a = \tau_b$. This fails to represent the morphological differences among different shapes.

a)

C=22.4 u
L=5.8 u

b)

C=22.4 u
L=5.8 u
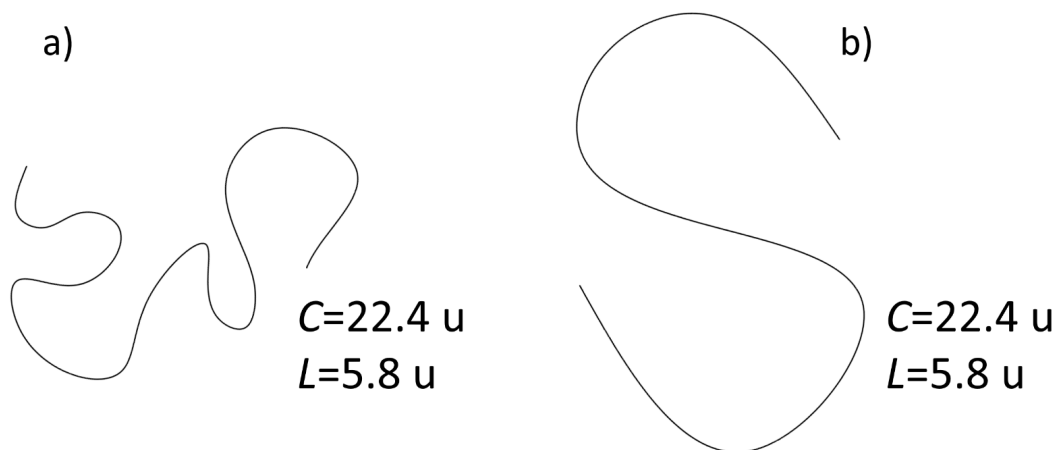
Figure 4.1: Example for curves with different morphological characteristics, same arc length and underlying chord.

Other methods have been proposed to compute the tortuosity of 2D structures. For instance, Chandrinos et al. [59] defined a measure based on computing the angle change

at discrete steps. Hart et al. [60] proposed a tortuosity τ involving curvature by segments. Goh et al. [61] presented a measure of τ based on the integration of all direction changes. Bullitt et al. [33] defined how to evaluate the number of inflection points (twists), in order to distinguish smoothly curved vessel from those ones that make abrupt changes in direction. Grisan et al. [62] proposed a novel method for the automatic grading of retinal vessel tortuosity. More recently, Bribiesca [36] proposed a measure of tortuosity for 2D curves represented by means of the Slope Chain Code (SCC). This representation is independent of translation, rotation, and optionally, of scaling, an important advantage for computing tortuosity. It also allows to use grammatical techniques to compute tortuosity in an easy way. An interesting review of quantifying the tortuosity of the retinal blood vessel was presented by M. Abdalla et al. [63].

In order to describe our proposed measure of tortuosity for voxelized objects, a number of concepts and definitions are presented below.

4.1 | Definitions

4.1.1 | Curvature

A curve is a continuous map from a one-dimensional space to an n-dimensional space. Latecki and Rosenfeld [64] presented an interesting approach to describe the boundaries of planar real objects by means of a class of planar arcs and curves. James and James [65] describe curvature as: "the absolute value of the rate of change of the angle of inclination of the tangent line with respect to distance along the curve". In the case of a circle the curvature is the reciprocal of the radius.

The curvature is an important element that allows the characterization of curves. The average curvature K_{av} of an *arc EF* is the ratio between the corresponding angle of contingency α, and the length of the arc (see Fig. 4.2a), which is equivalent to the geodesic distance between *EF* (Eq. 4.1),

$$K_{av} = \frac{\alpha}{EF} \tag{4.1}$$

The curvature K_E of a line at a given point E is the limit of the average curvature of *arcEF*, when the length of this arc approaches zero (that is, when point F approaches point E) and is defined as follows:

$$K_E = \lim_{F \to E} K_{av} = \lim_{EF \to 0} \frac{\alpha}{EF} \tag{4.2}$$

4.1.2 | Discrete curvature

When a curve is defined in the discrete space we can assume that the arc EF is constant and straight, as in the notation of the SCC [36]. Thus, if EF is equal to 1 in Eq. 4.1, then:

$$K_E = \alpha. \qquad (4.3)$$

Therefore, the *discrete curvature* of a discrete curve at point center G is the angle of contingency α, or the slope change between contiguous straight-line segments at that point. The slope change is scaled to lie within $(-1, 1)$. For practical purposes, we do not consider the slope changes equal to 1 or -1. Fig. 4.2b shows the range of slope changes $[0, 1)$ and $[0, -1)$.
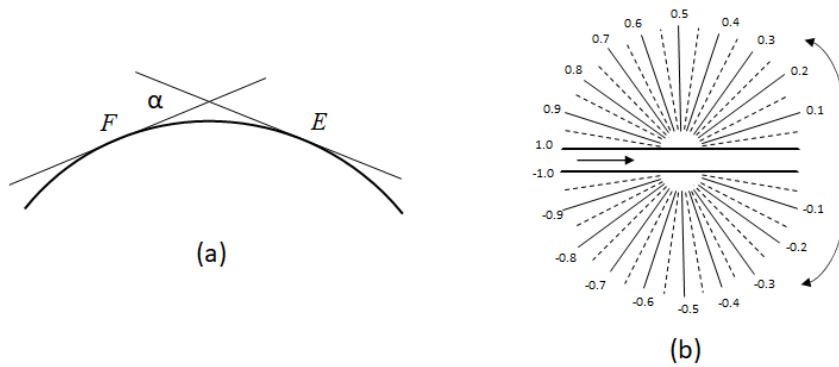
Figure 4.2: Curvature: (a) continuous curvature; (b) the range of slope changes $[0, 1)$ and $[0, -1)$.

4.1.3 | Slope chain code

The chain code is a contour oriented representation, based on region boundaries, resulting in a lossless data reduction of the image. The chain code of a region is determined by specifying a starting pixel and the sequence to go from pixel to pixel along the boundary [66].

Based on [36] a chain A is an ordered sequence of n elements, and is represented by Eq. 4.4

$$A = a_1 a_2 ... a_n \qquad (4.4)$$

When the element a_n of the chain represents the slope change of the contiguous straight-line segments of the curve in that element position, it is called a SCC. The range of slope changes varies from -1 to 1.

4.1.4 | 2D tortuosity

Tortuosity τ, a morphological property of curves and surfaces, is one of the most important measures of shape used to calculate deformations in different objects, allowing to quantify their degree of turns or detours. The definition for this work purposes is based on the SCC (Eq. 4.5), where τ is the sum of all the absolute values of the chain elements a_i and N is the number of elements [36].

$$\tau = \sum_{n=1}^{N} |a_n| \tag{4.5}$$

4.2 | Measure of τ_{3D}

The proposed estimation of tortuosity is designed to use a voxelized representation of a three-dimensional object as input.
The steps of the method are:

1. Obtain the voxelized representation of the object of interest.

2. Track contours for every slice i, j, k, for each corresponding direction X, Y, Z

3. Filter the stair-stepping artifact.

   - Design.
     - Downsample the contours.
     - Apply the Digital Straight Segment (DSS) algorithm [67].
   - Compute the 3D tortuosity of the resulting voxelized representation of the object of interest.

4. Uncertainty determination.

4.2.1 | Voxelized representation

The discrete representation of 3D objects has two different origins: voxelization and 3D reconstruction from multiple 2D images; in both cases the voxel is the volume unit.

The voxelization process consists in the approximation of data structures that store geometric information in a *continuous* domain by a set of voxels, i.e. the data of the object is now stored in a regular 3D grid [68].

The 3D reconstruction from multiple 2D images is a mathematical process that generates 3D models from multiple 2D projections. Reconstructed 3D images have become essential for the medical field (Magnetic Resonance Imaging, Computerized Tomography, Positron Emission Tomography), video games, robotics, augmented reality, computer vision, among others [69]. The reconstruction techniques depend on the acquisition methods.

4.2.2 | Contour tracking

To calculate the slope changes, the boundary of the voxelized object has to be approximated by straight-line segments. Contour tracking has the objective of tracing the complete border of an object and without repetition [70]; as a result, a boundary points sequence is obtained [71]. The object boundary provides the necessary information to analyze the shape and to estimate τ. For 3D objects, the contour tracking is performed for each slice s_i, and three directions X, Y and Z.

4.2.3 | Filtering the stair-stepping artifact

The main drawback for the voxelized representations comes from the stair-stepping artifact which, for measuring τ_{3D}, prevents obtaining the slope changes corresponding to the morphology of the object. In Fig. 4.3 a simple example of the stair stepping effect is presented. It shows a voxelized representation of a straight line in two different angles and the corresponding contour. The stair-stepping error, in this case, occurs when the angle is different from 0 or 90 degrees, which is shown in Fig. 4.3 right.

To accurately capture the morphology of the voxelized object. it is necessary to minimize the contribution of this artifact. We designed a two-step filter for this objective. First, we downsample the contour vertices, and second, we apply a DSS algorithm.
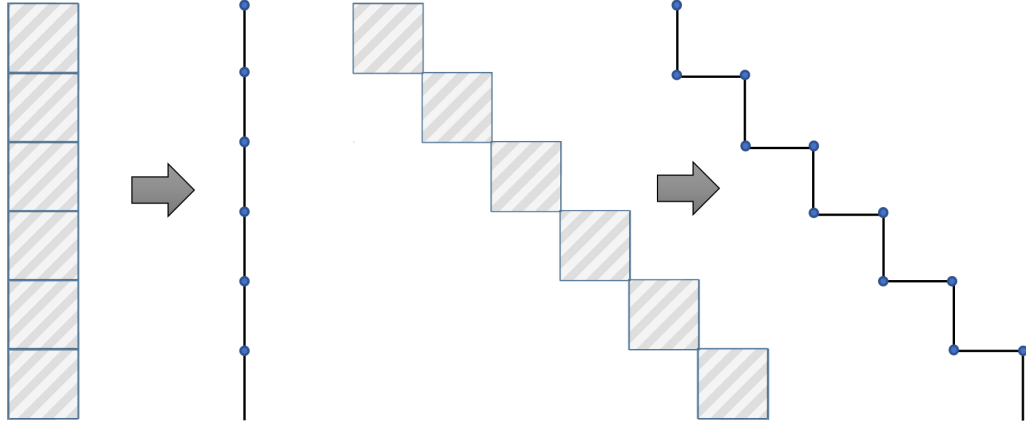
Figure 4.3: Example of the stair-stepping artifact. Left, voxelized representation of a straight line in a 90 degree angle and the corresponding contour. Right, voxelized representation of a straight line in a 45 degrees angle and the corresponding contour.

4.2.3.1 | Filter design

In this section, each step of the correction method and the uncertainty calculation is described. The uncertainty due to the stair-stepping artifact for the estimation of τ is quantified using a voxelized sphere as a computational phantom.

- *Downsampling contours.* To reduce the noise (stair-stepping artifact) the first step was to reduce by ten the sampling frequency of the tracked contours. The downsampling factor (DSW) is related to the size of the analyzed objects.

- *Digital straight segment algorithm.* After downsampling the contours the DSS algorithm is applied, to select the vertices that define different straight segments. DSS algorithms use a polygonal approximation to curves [72]. In this work the Kovalevsky [73] method was selected, it is based on the calculation of the narrowest strip defined by the nearest support below and above.

In Fig. 4.4 the steps of the designed filter are shown. A voxelized sphere was generated with a radius of 20 voxels and a 0° angle. The gray area is a slice of this sphere and the black line is the tracked contour. The downsample vertices are shown in blue and the results of the DSS algorithm are shown in red.
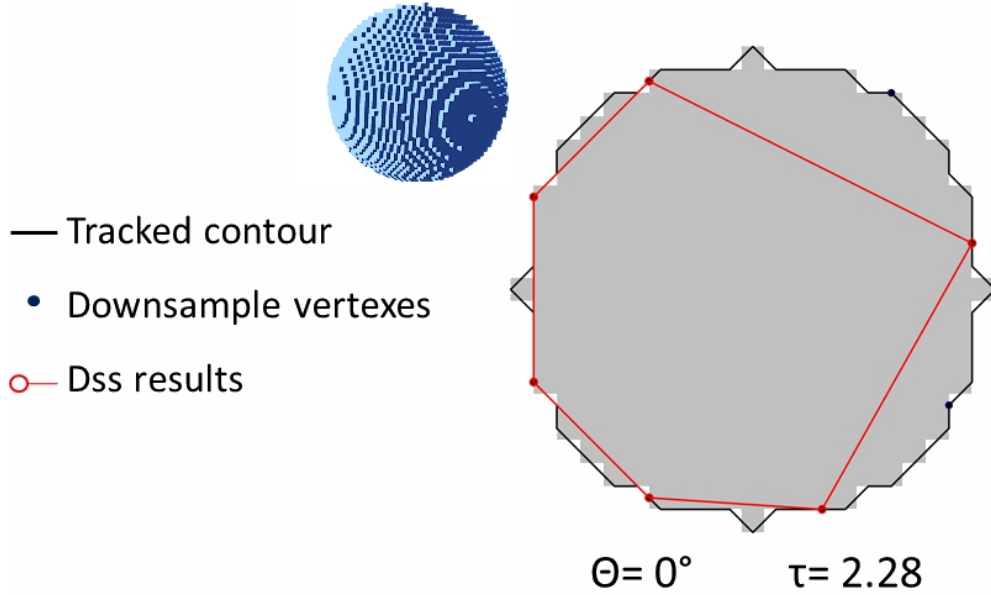
Figure 4.4: Filtered contour obtained from a sphere slice. The straight line is the tracked contour from the gray voxelized circle. The blue points are the downsample vertices and the red vertices are the result after apply the DSS algorithm.

4.2.4 | Tortuosity estimation

The 3D tortuosity estimation is proposed as an extension of the 2D measurement based on SCC, it consists of the sum of all the slope changes in each contour, in the three directions. The vertices of each contour are obtained after filtering the stair-stepping artifact (*with DSF=10 and the DSS algorithm*) to minimize its contribution to the tortuosity.

The equations presented in eq. 4.6 are the 3D adaptation of the chain element eq. 4.4 where N is the total number of chain elements, and S_X, S_Y, S_Z, represent the number of slices in each direction. Eq. 4.7 shows the correspondence between 2D tortuosity and 3D tortuosity computed per slice (i, j, k). The proposed equation to estimate τ_{3D} is presented in eq. 4.8, where N_i, M_j, L_k, are the number of chain elements, and slope change for each slice, and direction.

$$
\begin{aligned}
X_i &= x_{1i}x_{2i}...x_{Ni}, \text{ contour(s)in slice } i, \text{ direction } X, i = 1,...,S_X \\
Y_j &= y_{1j}y_{2j}...y_{Mj}, \text{ contour(s)in slice } j, \text{ direction } Y, j = 1,...,S_Y \\
Z_k &= z_{1k}z_{2k}...z_{Lk}, \text{ contour(s)in slice } k, \text{ direction } Z, k = 1,...,S_Z
\end{aligned}
\tag{4.6}
$$

$$\sum_{n=1}^{N_i} |a_n| \mapsto \sum_{n=1}^{N_i} |x_{ni}|, \sum_{m=1}^{M_j} |y_{mj}|, \sum_{l=1}^{L_k} |z_{lk}| \qquad (4.7)$$

$$\tau_{3D} = \frac{\displaystyle\sum_{i=1}^{S_X}\sum_{n=1}^{N_i} |x_{ni}|}{S_X} + \frac{\displaystyle\sum_{j=1}^{S_Y}\sum_{m=1}^{M_j} |y_{mj}|}{S_Y} + \frac{\displaystyle\sum_{k=1}^{S_Z}\sum_{l=1}^{L_k} |z_{lk}|}{S_Z} \qquad (4.8)$$

4.2.4.1 | Uncertainty

One of the propositions in the work of Bribiesca [36] is that the sum of the slope changes of simple closed curves always is equal to 2, in the three-dimensional case τ_{3D} is equal to 6. This allows to determine the uncertainty of the proposed method using a voxelized sphere.

The variation of τ_{3D} was evaluated in terms of the sphere radius and its generating angle, and determine the absolute error (Δx) for each measurement (x_i) comparing it with the true value (x), see eq. 4.9. In Fig. 4.5 the Δx of the estimated values of tortuosity changing the radius and angle is presented. $X-axis$ presents the different angles, in which the sphere is generated, from 0 to 360, $Y-axis$ has different sphere radii, from 10 to 80 voxels. The color bar represents the absolute error of τ_{3D}. The tortuosity can be estimated with an uncertainty of ± 1 for objects with $r \in [10, 70]$, and has proven to be invariant under scaling for DSF=10 (Fig. 4.5) ($\Delta x = |x_i - x|$). τ_{3D} is extremely sensitive to the chain elements definition, thus the filtering process is essential to an accurate estimation.

$$\Delta x = |x_i - x| \qquad (4.9)$$

43
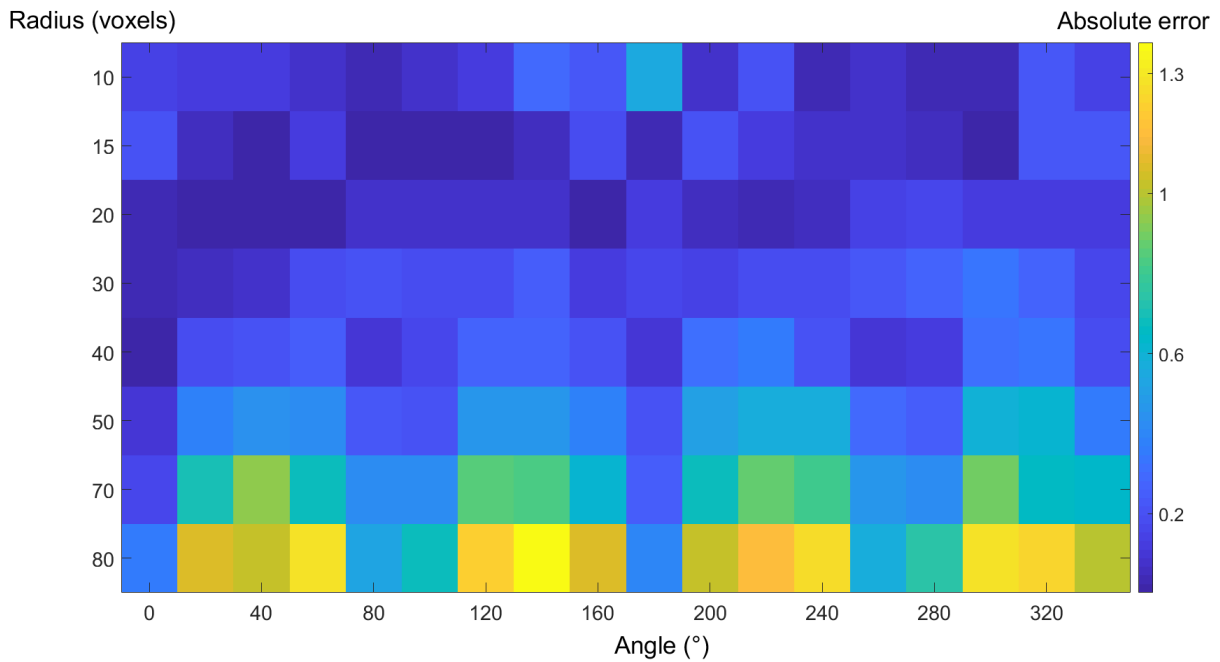
Figure 4.5: Tortuosity estimation for different radii. $Y-axis$, different radius sizes (pixels), $X-axis$, generating angle, color-scale, absolute error of estimated tortuosity.

4.3 | Application examples

To illustrate the potential of the proposed method, the τ_{3D} was estimated for different voxelized objects: an hippocampus, a volcano and the brain. The proposed method was successfully applied to the three presented examples, the results are shown in Figs. 4.6, 4.7 and 4.8.

In the first example (Fig.4.6) the tortuosity is used to compare the morphology of two hippocampi from different patients. On the left, an axial view of the brain with the hippocampus labeled in red; the two different views of the hippocampi are shown with the respective value of τ_{3D}. The morphological differences can be described qualitatively, and the tortuosity allows to quantify them, and to differentiate between this two hippocampi,

44
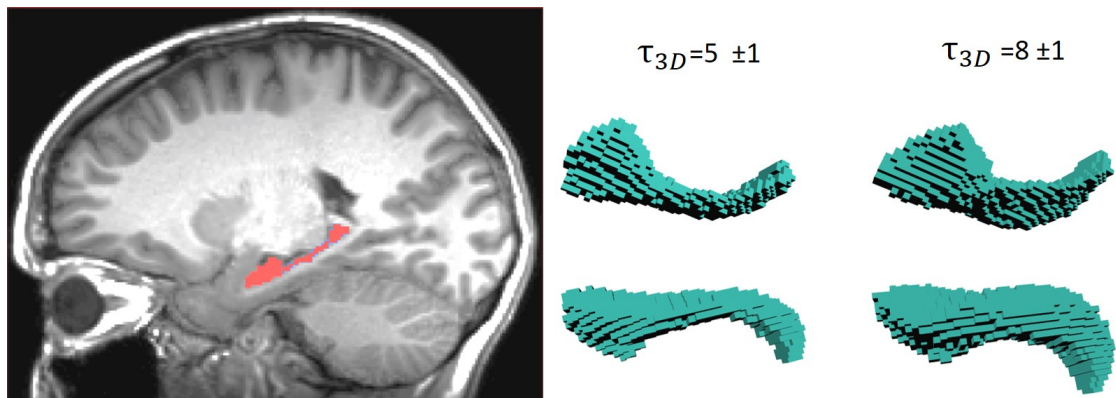
Figure 4.6: Left,a coronal view of a brain MRI with the hippocampus labeled. Right, two views pf different voxelized hippocampi, and the respective τ_{3D} estimation.

The second example is a voxelized representation of the Iztaccihuatl (a Mexican volcano). Three different 2D orthogonal projections are shown (XY, XZ and YZ), in each case the blue line is the tracked contour, ant the red circles are the result of the stair-stepping artifact filter, which are used to compute τ_{3D}. For this kind of images the proposed descriptor can help to evaluate the morphological differences between volcanoes, the possibles changes after volcanic activity, the changes in time of the surface, among natural changes of the environment.

τ_{3D}=12.2 ±1
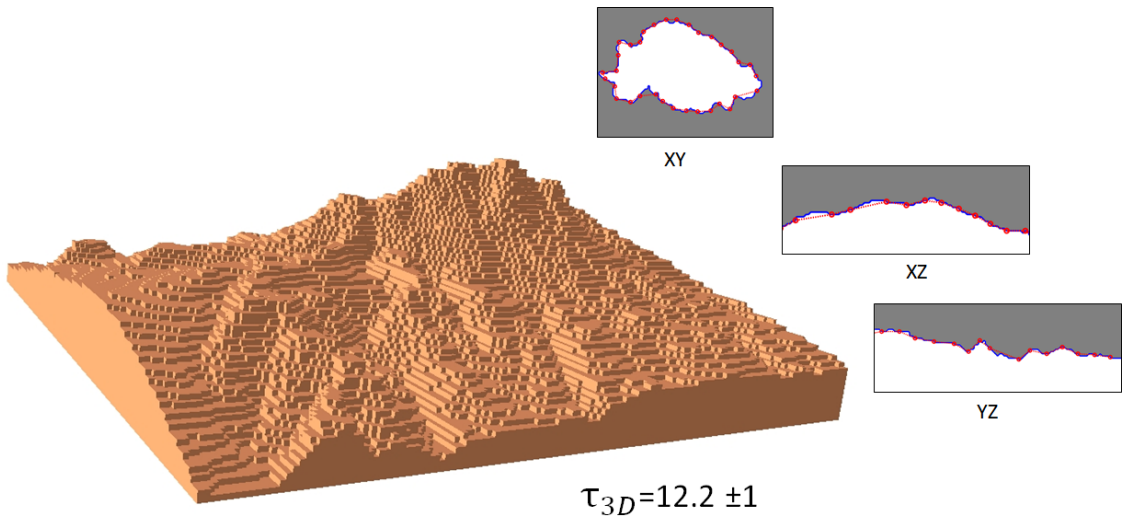
Figure 4.7: Voxelized model of the Iztaccihuatl volcano with the τ_{3D} estimation. On the left three different slices projected in orthogonal planes are shown. Each slice show the projection of the voxelized volcano in the respective plane, the tracked contour with a blue line, and the filtered vertices with red circles.

The third example consists of a magnetic resonance study of the brain and the result after applying the closing operation with different sizes of the structuring element. The brain surface is extracted to appreciate the gray matter morphology, particularly its tortuosity. In this example we use five different volumes, which correspond to the same subject (Fig. 4.8). The first case is the original voxelized brain surface, the other four are the result of applying the Mathematical Morphology operator of *closing*, defined in Eq. 4.10, using a sphere as the structuring element B, with different radii ($r \in \{2, 4, 6, 8\}$). The morphological closing of a binary image I by a structuring element B is a composition of a dilation ($\oplus$) an erosion ($\ominus$). When applied to 2D or 3D images, this operator is used to fill holes, reduce concavities, and smooth rough features.
The increment of the structuring element radius results in the loss of feature details on the brain surface (the gyri and the sulci), therefore, a decrease in the values of τ_{3D} is expected.

$$(I \oplus B) \ominus B \qquad (4.10)$$

46

Original brain volume	Brain closing with sphere of r=2	Brain closing with sphere of r=4	Brain closing with sphere of r=6	Brain closing with sphere of r=8

3D Tortuosity				
50.376	27.040	14.197	10.084	8.699
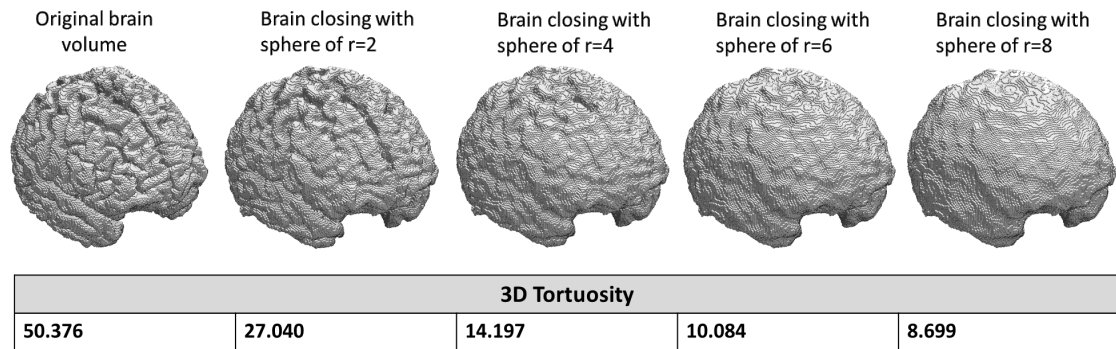
Figure 4.8: Top: brain volumes after applying the Mathematical Morphology operator of "closing" (Eq. 4.10) with five structuring elements: a sphere with increasing radii. Bottom: the corresponding estimated values of 3D tortuosity.

4.4 | Central sulcus tortuosity estimation

4.4.1 | Overview

As mention before studies of brain morphometry using MRI are still relevant because they have shown potential for the prognosis of neurological disease. Particularly, cortical folding structure (gyrus and sulci) is a current field of study and the most analyzed morphological descriptors are the sulcal width (SW) and the cortical thickness [74]. Nevertheless, there is a lot more information that can be extracted from the anatomical MRI images to characterize the sulci. In this chapter, the 3D tortuosity of the central sulcus is calculated for the subjects in Minimal Interval Resonance Imaging in the Alzheimer's Disease (MIRIAD) database. The tortuosity is a morphological property of an object being twisted or having many turns.

In the case of the central sulcus the tortuosity can give information about the folding pattern differences between hemispheres, or among populations with different pathologies, especially in neurodegenerative diseases. It is important to remember that the folding patterns are related to the brain's functional organization. Thus, the hypothesis of this work is that the calculation of the 3D tortuosity of the central sulcus captures morphological changes of the pial surface structure caused by the gray matter loss in Alzheimer patients. This work has been published in the Nuclear Science Symposium and Medical Imaging Conference [75].

47

4.4.2 | Central sulcus implementation

The 3D tortuosity Slope Chain Code based method aims to measure the tortuosity and use it as a morphological descriptor, and possible biomarker for the central sulcus. This descriptor is calculated for the enveloping surface of the sulcus.

First, the pial surface was extracted employing the FreeSurfer cross-sectional pipeline to each structural T1-weighted MRI scan. To label the central sulcus, the Destrieux Atlas (2009) and the morphological closing of the pial surface obtained with a sphere with a radius of 3 voxels as the structuring element, were employed. The central sulcus is extracted for each hemisphere and each subject. In order to measure τ the proposed method is followed.

Left Central Sulcus

τ= 6.82   τ= 1.23
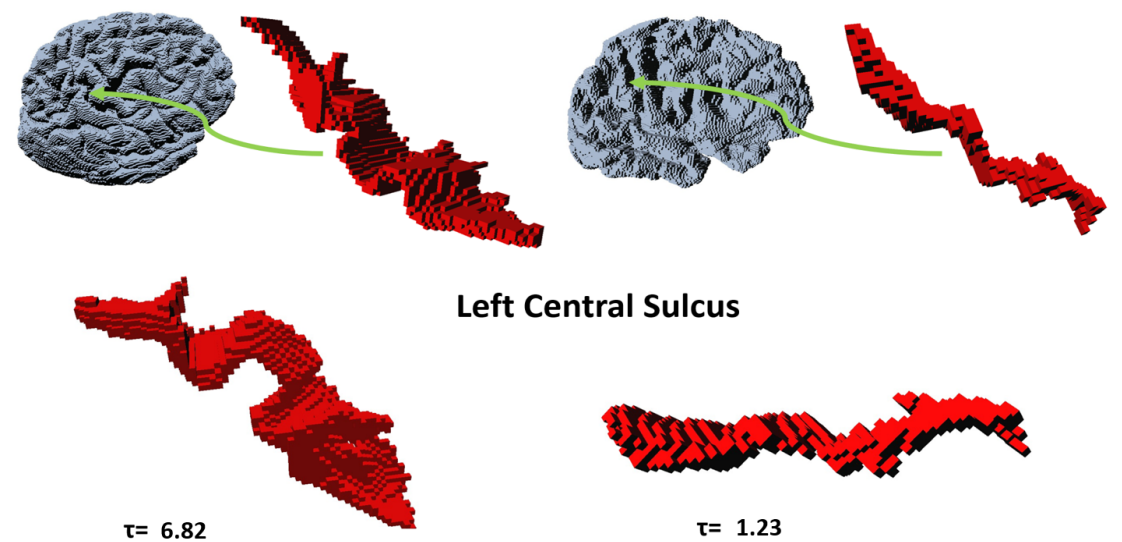
Figure 4.9: Two different central sulci of different subjects, both from the left hemisphere. Right, the voxelized volume of a patient with AD and the maximum value of tortuosity. Left, the voxelized volume of a control subject with the minimum value of tortuosity

The tortuosity was computed for the central sulci of 66 subjects: 43 patients with AD and 23 control subjects of the Minimal Interval Resonance Imaging in AD database (MIRIAD), a set of high-resolution MR images.

4.4.3 | Results

As it is known AD causes significant gray matter loss; hence it was expected to cause morphological changes among sulci. The tortuosity was compared between the central sulci in both hemispheres and between controls and AD patients. The central sulcus was chosen because it is well defined, easy to label and it has been shown that its morphology is related to the Alzheimer disease [76], [23]. The results of the method were consistent with this hypothesis.

In Fig. 4.9 the maximum and minimum values of τ are presented, with their corresponding voxelized representation of the central sulcus of each subject. The result of the Wilcoxon tests show that the tortuosity values of the central sulci are significantly larger for the AD patients ($p < 0.05$) for both hemispheres.

AD patients vs.Control Subjects	Left-hemisphere	Right-hemisphere
p-values	0.021	0.21
z-values	2.32	1.26

Table 4.1: Results of the Wilcoxon tests applied to the tortuosity of the central sulci of each hemisphere.

In table 4.1 the results of the Wilcoxon test preformed to the tortuosity values obtained for the central sulcus are shown for each hemisphere. The null hypothesis is rejected only for the central sulci on the left-hemisphere, and the z-value indicates that grater for the AD patients.

While the tortuosity values obtained for the central sulci on the right hemisphere cannot be differentiated between AD patients and control subjects. We also compare the central sulcus morphology between hemispheres, the results are shown in 4.2.

The results presented on table 4.2 show that, the values of tortuosity of the central

	AD patients Left-Right hemispheres	Control Subjects Left-Right hemispheres
p-values	5.19e-06	6.12e-07
z-values	-4.56	-4.99

Table 4.2: Results of the Wilcoxon tests applied to the tortuosity of the central sulci of each hemisphere.

sulci on the left hemisphere, are significantly different than the values for the right hemisphere, in both cases (AD patients and Control subjects). The sign on the z-value

shows that the vales for the central sulci located in the left hemisphere are lower than the values for the right hemisphere.

4.5 | Discussion

A method of tortuosity an SCC-based was chosen among the other because it is invariant under translation, rotation, and scale, also it allows a unidimensional representation of curves. As mention before, tortuosity has been used for many applications and it has helped to describe different phenomena, mainly for the medical field.

The three-dimensional tortuosity has been proposed by Peyrega, Pardo-Alonso and Gommes Cedric ([77], [78] and [79]), all of them work on porous media, Peyrega et. al. ([77]) defines the tortuosity as the ratio between the geodesic distance from each voxel to two different subsets of the object and the Euclidean distance between them. As a result each voxel has a tortuosity value, they use these tortuosity values to connect a geodesic path. The method was developed for a particular application for 3D images of fibrous material, in which entry and exit points can be defined, in consequence, it can not be applied to other volumetric objects. Pardo-Alonso et. al. compared four different approaches to compute the geometrical tortuosity in infiltrated aluminum cellular materials, all estimation methods evaluated were based on the definition of tortuosity as the ratio in between geodesic distance and the Euclidean distance, the differences among them is the definition of the paths through the material.

Gomes Cedric et. al. ([79]) proposed measures of tortuosity of porous materials from binary or gray-tone reconstructions. The first approach is based on a direct comparison of the geodesic and Euclidean distances calculated from any pore pixel to any limit of the tomogram. The second method, is based on the geodesic reconstruction of the pore space of the tomogram, starting from any of its limits, and considering its intensity variations. The three methods aforementioned were developed for a particular kind of phenomena, although they work with 3D objects, the tortuosity, as defined by those authors, it is not meant to capture the 3D morphological changes of volumetric objects, it describes the changes in 3D trajectories. Because of the indicated differences the methods can not be compared.

The motivation to extend the 2D SCC based approach for 3D objects is to describe and quantify the morphological changes describing the complexity of volumetric objects.

An advantage of the proposed method to estimate τ_{3D} is applying a simple algorithm, based on the SCC representation of the object. The information to generate the SCC is obtained directly from the voxels (without interpolation), and it results in reducing the sources of uncertainty. Another advantage is that It can be used for any voxelized object, allowing its use in many fields. The presented examples explore some of the possible ways in which the estimation of $\tau_3 D$ can enrich the descriptions of the analyzed object.

5

Conclusions

This thesis presents two descriptors and their application to measure morphological characteristics of brain structures. First, a novel voxel-based method for measuring sulcal width and extracting descriptors to characterize and compare sulci within and among brains. This tool can be applied to analyze different populations, especially those with neurodegenerative diseases. Few similar algorithms have been developed, and the main advantage of this method is that it is easy to implement, and it generates sulcal width maps, which can be used to qualitatively analyze the entire brain or only selected sulci.

Second, the tortuosity for 3D voxelized objects based on the slope chain code, the approach for 2D curves was proposed by Bribiesca [36]. τ_{3D} is presented as the normalized sums of all the slope chain elements for each filtered contour, every slice, and direction X, Y, and Z (Eq.4.8). A filter, to minimize the effect of the stair-stepping artifact on the 3D tortuosity estimation, was proposed and evaluated. We were able to validate the obtained values of τ and calculate the accuracy. The DSF value was selected to maximize the τ_{3D} accuracy, and resolution. It was found that the optimal DSF value is 10 and the minimum radius of the object to analyze is 10. Measuring this descriptor in 3D voxelized objects represents a great advantage, we were able to measute and compare the central sulcus τ_{3D} using the MIRIAD database, we found a significan difference between left and right hemisphere τ_{3D} for both, control subjects and AD patients. Also we found that the obtained values of τ_{3D} for the central sulci located in the left-hemisphere are different between AD patients and control subjects, the values for the right-hemisphere are not significantly different. this shows the potential relevance of τ_{3D} to study sulci.

One of the main contribution of this thesis the use of computational phantoms to

validate the proposed methods. The validation allows to know the conditions in which the algorithm can be used and its accuracy, this is absolutely necessary to obtain a valid quantification.

The descriptors presented in this work are able to quantify different shape characteristics of the brain folding patters, which has two direct consequences: first, they can be used to characterize and describe different populations, and second, they have the potential to be used as biomarkes for some brain conditions.

Further work may involve applying these descriptors to a larger databases and testing them in terms of aging and other neurodegenerative diseases. Also improve the Local Maxima labeling algorithm to fill voids of the 3D crest lines, allowing a voxel-wise approach. In the case of $\tau 3D$ one of the main issues when it comes to the application in the sulci, is the accurate segmentation of the region of interest, also further work may include a way to normalize the tortuosity in order to compare it among significantly different structures.

Helicoidal horn construction

In this section we present the analytical construction of the helicoidal horn. It is important to clarify that is not intended to be a representation of the a brain sulcus, its main objective is to model the sulci variations: direction (x, y and z) and width changes.

A.1 | Distance of a Point to a Circle

In Fig. A.1 an axis ring of the helicoidal horn is presented as well as the points and segments definitions, necessary for its construction. The following relations and equations give us the elments to define the distance of a given point **P** to the circle.
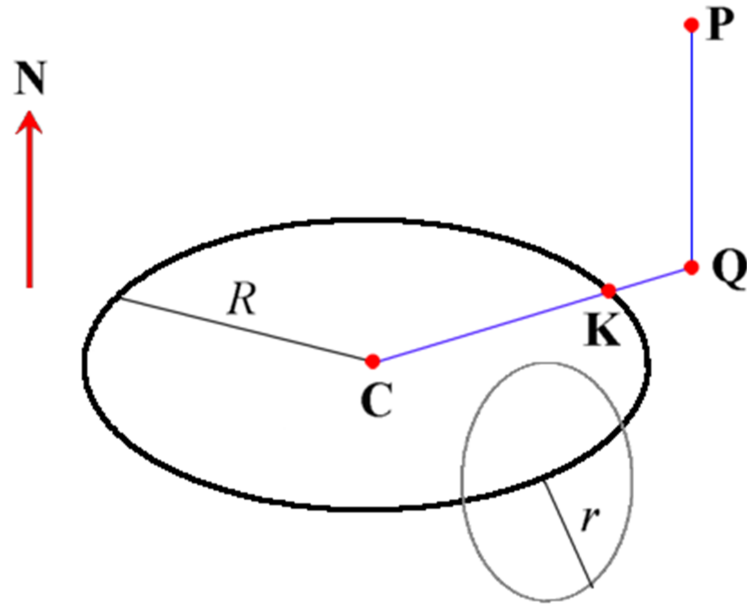
Figure A.1: Circular horn-axis ring and point/vector definitions and relations.

		C code variable name
C	Center of the circular ring-axis of the toroid.	C_x, C_y, C_z
R	Major radius of a toroid (main circular ring-axis).	R_{axis}
r	Minor radius of a toroid (cross section disk).	$R_{transversal}$
N	Normal vector of the plane of the circle, $\|N\| = 1$.	N_x, N_y, N_z
P	Any point in 3D.	x, y, z
Q	Projection of P onto the plane of the circle.	Q_x, Q_y, Q_z
K	Circle point closest to P. Points C, K, Q, P are co-planar.	K_x, K_y, K_z

$$\mathbf{Q} - \mathbf{C} = \mathbf{P} - \mathbf{C} - (\mathbf{N} \cdot (\mathbf{P} - \mathbf{C}))\mathbf{N} \Rightarrow \mathbf{P} - \mathbf{Q} = (\mathbf{N} \cdot (\mathbf{P} - \mathbf{C})\mathbf{N} \tag{A.1}$$

$$\mathbf{K} = \mathbf{C} + \mathbf{R}\frac{\mathbf{Q} - \mathbf{C}}{\|\mathbf{Q} - \mathbf{C}\|} = \mathbf{C} + \mathbf{R}\frac{(\mathbf{P} - \mathbf{C} - (\mathbf{N} \cdot (\mathbf{P} - \mathbf{C}))\mathbf{N})}{\|(\mathbf{P} - \mathbf{C} - (\mathbf{N} \cdot (\mathbf{P} - \mathbf{C}))\mathbf{N})\|} \tag{A.2}$$

The points K, Q, P form a right triangle, thus the squared (minimal) distance between

a point P and a circle is:

$$
\begin{aligned}
d^2 &= \|\mathbf{P} - \mathbf{K}\|^2 = \|\mathbf{P} - \mathbf{Q}\|^2 + \|\mathbf{Q} - \mathbf{K}\|^2 \\
&= (\mathbf{N} \cdot (\mathbf{P} - \mathbf{C}))^2 + (\|\mathbf{Q} - \mathbf{C}\| - \mathbf{R})^2 \\
&= \boxed{(\mathbf{N} \cdot (\mathbf{P} - \mathbf{C}))^2 + (\sqrt{(\mathbf{P} - \mathbf{C})^2 - (\mathbf{N} \cdot (\mathbf{P} - \mathbf{C}))^2} - \mathbf{R})^2}
\end{aligned} \tag{A.3}
$$

A.2 | Distance of a Point to a Helix (a curved cone)

In Fig. A.2 is the 3D extension of the previous case, in which we define the distance from a point **P** to a helix.

Figure A.2: Helicoidal horn-axis ring and point/vector definitions and relations.

		Ccodevariablename
θ	The arc-of-length parameter, in radians.	*theta*
$\mathbf{R_{axis}}$	Major radius of the helix at θ (main circular ring-axis).	R_{axis}
$\mathbf{r}$	Rate of the helix "elevation", or $pitch = 2\pi b$ and $slope = b/Raxis$	b
$\mathbf{C_{helix}}(\theta)$	Center of the circular ring-axis of the helix at θ.	C_x, C_y, C_z
$\mathbf{C_{helix}}(0)$	Initial center values.	C_x, C_y, C_z
$\mathbf{r_{transversal}}(\theta)$	Transversal (cross-section) radius of the toroidal or horn helix at θ.	$R_{transversal}$
$\mathbf{T}(\theta)$	Tangential vector of the helix, $\|\mathbf{T}\| = \mathbf{1}$.	$Tang_x, Tang_y, Tang_z$
$\mathbf{N}(\theta)$	Normal vector of the helix, $\|\mathbf{T}\| = \mathbf{1}$.	$Norm_x, Norm_y, Norm_z$
	$\mathbf{T}, \mathbf{N}$ define the osculating plane at θ. (N is also named the curvature vector)	
$\mathbf{B}(\theta)$	Binormal vector of the helix, $\|\mathbf{B}\| = \mathbf{1}$.	$Binorm_x, Binorm_y, Binorm_z$
	$\mathbf{B}$ is orthogonal to the osculating plane of the helix at θ	
	$\mathbf{T}, \mathbf{N}, \mathbf{B}$ is a trihedron at any point of the helix at θ	
$\mathbf{P}$	Any point in 3D.	x, y, z
	To calculate the distance of $\mathbf{P}$ to the helix, we obtain its argument wrt $\mathbf{C_{helix}}$	
	$\theta = atan2(y - C_y, x - C_x) + \pi$, with positive range $\pi \in [0, 2\pi]$	
$\mathbf{Q}$	Projection of $\mathbf{P}$ onto the osculating plane of the helix at θ, following $B(\theta)$	
$\mathbf{K}(\theta)$	Helix point closest to $\mathbf{P}$.	K_x, K_y, K_z
	Note that points $\mathbf{C_{helix}}, \mathbf{K}, \mathbf{Q}, \mathbf{P}$ are "instantaneously" co-planar for any θ.	
$\mathscr{H}(\theta)$	Parametrical definition of the helix:	$Helix(theta)$

$$\mathscr{H}(\theta) = \begin{cases} R_{axis}\cos(\theta) + C_x \\ R_{axis}\sin(\theta) + C_y \\ C_z + b\,\theta \end{cases} \qquad (A.4)$$

$$\mathbf{T}_{unorm}(\theta) = \frac{d\mathscr{H}(\theta)}{d\theta} = \begin{cases} -R_{axis}\sin(\theta) \\ R_{axis}\cos(\theta) \\ b \end{cases}, \quad \mathbf{T} = \frac{\mathbf{T}_{unorm}}{\|\mathbf{T}_{unorm}\|} \qquad (A.5)$$

$$\mathbf{N}_{unorm}(\theta) = \frac{d\mathbf{T}(\theta)}{d\theta} = \begin{cases} -R_{axis}\cos(\theta) \\ -R_{axis}\sin(\theta) \\ 0 \end{cases}, \quad \mathbf{N} = \frac{\mathbf{N}_{unorm}}{\|\mathbf{N}_{unorm}\|}, \qquad (A.6)$$

where $\mathbf{N} \cdot \mathbf{T} = 0$, $\mathbf{N} = \mathbf{T}^{\perp}$ in the osculating plane, $\mathbf{N}(\theta)$ points to $\mathbf{Chelix}(\theta)$, and:

$$\mathbf{B}(\theta) = \mathbf{T}(\theta) \times \mathbf{N}(\theta) \qquad (A.7)$$

The shortest distance follows the same formulation as in the case $b = 0$, at any θ :

$$\mathbf{Q} - \mathbf{C}_{helix} = \mathbf{P} - \mathbf{C}_{helix} - (\mathbf{B} \cdot (\mathbf{P} - \mathbf{C}_{helix}))\mathbf{B} \implies \mathbf{P} - \mathbf{Q} = (\mathbf{B} \cdot (\mathbf{P} - \mathbf{C}_{helix}))\mathbf{B}, \quad (A.8)$$

$$\mathbf{K} = \mathbf{C}_{helix} + R_{axis}\frac{\mathbf{Q} - \mathbf{C}_{helix}}{\|\mathbf{Q} - \mathbf{C}_{helix}\|} = \mathbf{C}_{helix} + R_{axis}\frac{\mathbf{P} - \mathbf{C}_{helix} - (\mathbf{B} \cdot (\mathbf{P} - \mathbf{C}_{helix}))\mathbf{B}}{\|\mathbf{P} - \mathbf{C}_{helix} - (\mathbf{B} \cdot (\mathbf{P} - \mathbf{C}_{helix}))\mathbf{B}\|} \quad (A.9)$$

The points $\mathbf{K}, \mathbf{Q}, \mathbf{P}$ form a right triangle, thus the squared (minimal) distance between a point P and an helix $\mathbf{Heli}(\theta)$ is:

$$
\begin{aligned}
d^2 &= \|\mathbf{P} - \mathbf{K}\|^2 = \|\mathbf{P} - \mathbf{Q}\|^2 + \|\mathbf{Q} - \mathbf{K}\|^2 \\
&= (\mathbf{B} \cdot (\mathbf{P} - \mathbf{C}_{helix}))^2 + (\|\mathbf{Q} - \mathbf{C}_{helix}\| - R_{axis})^2 \\
&= \boxed{(\mathbf{B} \cdot (\mathbf{P} - \mathbf{C}_{helix}))^2 + (\sqrt{(\mathbf{P} - \mathbf{C}_{helix})^2 - (\mathbf{B} \cdot (\mathbf{P} - \mathbf{C}_{helix}))^2} - R_{axis})^2}
\end{aligned}
\tag{A.10}
$$

The helix torsion τ is defined as:

$$
\tau = \frac{(\mathscr{H}' \times \mathscr{H}'') \cdot \mathscr{H}'''}{\|\mathscr{H}' \times \mathscr{H}''\|}, \qquad \mathscr{H}(\theta) = \begin{cases} u = R_{axis}\cos(\theta) \\ v = R_{axis}\sin(\theta) \\ w = b\theta \end{cases}
\tag{A.11}
$$

with,

$$
\tau = \frac{u'''(v'w'' - v''w') + v'''(w'u'' - w''u') + w'''(u'v'' - u''v')}{(v'w'' - v''w')^2 + (w'u'' - w''u')^2 + (u'v'' - u''v')^2} = \boxed{\frac{b}{R_{axis}^2 + b^2}}
\tag{A.12}
$$

and its curvature κ:

$$
if\ b = 0\ (a\ circle),\ then \qquad \kappa = \frac{1}{R_{axis}}
\tag{A.13}
$$

The analytical solution of the distance calculation of a given point $\mathbf{P}$ to the helicoidal horn is given, thus, for any given point we can calculate the exact distance, and compare it with the result of the proposed method for calculating the sulci width in a voxel representation of the brain from MRI images.

References

[1]   J. P. Wansapura, S. K. Holland, R. S. Dunn, and W. S. Ball Jr, "Nmr relaxation times in the human brain at 3.0 tesla," *Journal of Magnetic Resonance Imaging: An Official Journal of the International Society for Magnetic Resonance in Medicine*, vol. 9, no. 4, pp. 531–538, 1999.

[2]   K. Doi, "Diagnostic imaging over the last 50 years: research and development in medical imaging science and technology," *Physics in Medicine & Biology*, vol. 51, no. 13, p. R5, 2006.

[3]   A. P. Dhawan, *Medical image analysis*.   John Wiley & Sons, 2011, vol. 31.

[4]   R. Bansal, A. J. Gerber, and B. S. Peterson, "Brain morphometry using anatomical magnetic resonance imaging," *Journal of the American Academy of Child and Adolescent Psychiatry*, vol. 47, no. 6, p. 619, 2008.

[5]   J.-F. Mangin, D. Riviere, A. Cachia, E. Duchesnay, Y. Cointepas, D. Papadopoulos-Orfanos, D. L. Collins, A. C. Evans, and J. Régis, "Object-based morphometry of the cerebral cortex," *IEEE transactions on medical imaging*, vol. 23, no. 8, pp. 968–982, 2004.

[6]   P. Kochunov, W. Rogers, J.-F. Mangin, and J. Lancaster, "A library of cortical morphology analysis tools to study development, aging and genetics of cerebral cortex," *Neuroinformatics*, vol. 10, no. 1, pp. 81–96, 2012.

[7]   S. Alcauter, F. A. Barrios, R. Díaz, and J. Fernández-Ruiz, "Gray and white matter alterations in spinocerebellar ataxia type 7: an in vivo dti and vbm study," *Neuroimage*, vol. 55, no. 1, pp. 1–7, 2011.

[8]   H. Matsuda, "Voxel-based morphometry of brain mri in normal aging and alzheimer's disease," *Aging and disease*, vol. 4, no. 1, p. 29, 2013.

[9]   R. Damadian, "Tumor detection by nuclear magnetic resonance," *Science*, vol. 171, no. 3976, pp. 1151–1153, 1971.

[10]   P. C. Lauterbur *et al.*, "Image formation by induced local interactions: examples employing nuclear magnetic resonance," 1973.

[11] P. A. Bottomley, H. Hart Jr, W. Edelstein, J. Schenck, L. Smith, W. Leue, O. Mueller, and R. Redington, "Anatomy and metabolism of the normal human brain studied by magnetic resonance at 1.5 tesla." *Radiology*, vol. 150, no. 2, pp. 441–446, 1984.

[12] M. Johnson, J. Pennock, G. Bydder, R. Steiner, D. Thomas, R. Hayward, D. Bryant, J. Payne, M. Levene, and A. Whitelaw, "Clinical nmr imaging of the brain in children: normal and neurologic disease," *American Journal of Roentgenology*, vol. 141, no. 5, pp. 1005–1018, 1983.

[13] B. A. Holland, D. K. Haas, D. Norman, M. Brant-Zawadzki, and T. H. Newton, "Mri of normal brain maturation." *American Journal of Neuroradiology*, vol. 7, no. 2, pp. 201–208, 1986.

[14] T. Ai, J. N. Morelli, X. Hu, D. Hao, F. L. Goerner, B. Ager, and V. M. Runge, "A historical overview of magnetic resonance imaging, focusing on technological innovations," *Investigative radiology*, vol. 47, no. 12, pp. 725–741, 2012.

[15] M. Lakrimi, A. Thomas, G. Hutton, M. Kruip, R. Slade, P. Davis, A. Johnstone, M. Longfield, H. Blakes, S. Calvert *et al.*, "The principles and evolution of magnetic resonance imaging," in *Journal of Physics: Conference Series*, vol. 286, no. 1.   IOP Publishing, 2011, p. 012016.

[16] G. B. Frisoni, N. C. Fox, C. R. Jack Jr, P. Scheltens, and P. M. Thompson, "The clinical use of structural mri in alzheimer disease," *Nature Reviews Neurology*, vol. 6, no. 2, p. 67, 2010.

[17] A. M. Fjell, L. McEvoy, D. Holland, A. M. Dale, K. B. Walhovd, A. D. N. Initiative *et al.*, "What is normal in normal aging? effects of aging, amyloid and alzheimer's disease on the cerebral cortex and the hippocampus," *Progress in neurobiology*, vol. 117, pp. 20–40, 2014.

[18] L. H. Somerville, "Searching for signatures of brain maturity: what are we searching for?" *Neuron*, vol. 92, no. 6, pp. 1164–1167, 2016.

[19] P. Gautam, K. J. Anstey, W. Wen, P. S. Sachdev, and N. Cherbuin, "Cortical gyrification and its relationships with cortical volume, cortical thickness, and cognitive performance in healthy mid-life adults," *Behavioural brain research*, vol. 287, pp. 331–339, 2015.

[20] B. Fischl, N. Rajendran, E. Busa, J. Augustinack, O. Hinds, B. T. Yeo, H. Mohlberg, K. Amunts, and K. Zilles, "Cortical folding patterns and predicting cytoarchitecture," *Cerebral cortex*, vol. 18, no. 8, pp. 1973–1980, 2007.

[21] K. Hoehn and E. N. Marieb, *Human anatomy & physiology*.   Benjamin Cummings, 2007.

[22] D. Van Essen and H. Drury, "Structural and functional analyses of human cerebral cortex using a surface-based atlas," *Journal of Neuroscience*, vol. 17, no. 18, pp. 7079–7102, 1997.

[23] T. Liu, D. M. Lipnicki, W. Zhu, D. Tao, C. Zhang, Y. Cui, J. S. Jin, P. S. Sachdev, and W. Wen, "Cortical gyrification and sulcal spans in early stage alzheimer's disease," *PloS one*, vol. 7, no. 2, p. e31083, 2012.

[24] L. Lee, E. Dale, A. Staniszewski, H. Zhang, F. Saeed, M. Sakurai, I. Orozco, F. Michelassi, N. Akpan, H. Lehrer *et al.*, "Regulation of synaptic plasticity and cognition by sumo in normal physiology and alzheimer's disease," *Scientific reports*, vol. 4, p. 7190, 2014.

[25] D. Liu and F. Xia, "Assessing object-based classification: advantages and limitations," *Remote Sensing Letters*, vol. 1, no. 4, pp. 187–194, 2010.

[26] J.-F. Mangin, E. Jouvent, and A. Cachia, "In-vivo measurement of cortical morphology: means and meanings," *Current opinion in neurology*, vol. 23, no. 4, pp. 359–367, 2010.

[27] I. Martínez Tejada, "Vertexwise sulcal width map computed over the human cortical surface using magnetic resonance imaging," B.S. thesis, 2016.

[28] S. N. Srihari, "Representation of three-dimensional digital images," *ACM Computing Surveys (CSUR)*, vol. 13, pp. 399–424, 12 1981. [Online]. Available: https://dl.acm.org/doi/10.1145/356859.356862

[29] J. K. Udupa, "Three-dimensional visualization and analysis methodologies: A current perspective," pp. 783–806, 5 1999.

[30] R. Weiner, *Webster's new world dictionary of media and communications*, 1990, no. Sirsi) i9780139697593.

[31] L. H. Le, C. Zhang, D. Ta, and E. Lou, "Measurement of tortuosity in aluminum foams using airborne ultrasound," *Ultrasonics*, vol. 50, no. 1, pp. 1–5, 2010.

[32] R. Annunziata, A. Kheirkhah, S. Aggarwal, P. Hamrah, and E. Trucco, "A fully automated tortuosity quantification system with application to corneal nerve fibres in confocal microscopy images," *Medical image analysis*, vol. 32, pp. 216–232, 2016.

[33] E. Bullitt, G. Gerig, S. M. Pizer, W. Lin, and S. R. Aylward, "Measuring tortuosity of the intracerebral vasculature from mra images," *IEEE transactions on medical imaging*, vol. 22, no. 9, pp. 1163–1171, 2003.

[34] T. Zhang and G. Nagy, "Surface tortuosity and its application to analyzing cracks in concrete," in *Proceedings of the 17th International Conference on Pattern Recognition, 2004. ICPR 2004.*, vol. 2. IEEE, 2004, pp. 851–854.

[35] W. Xiao, C. Xia, W. Wei, and Y. Bian, "Combined effect of tortuosity and surface roughness on estimation of flow rate through a single rough joint," *Journal of Geophysics and Engineering*, vol. 10, no. 4, p. 045015, 2013.

[36] E. Bribiesca, "A measure of tortuosity based on chain coding," *Pattern recognition*, vol. 46, no. 3, pp. 716–724, 2013.

[37] S. Sharma and M. Majsak, "Brain anatomy," 2014.

[38] P. Hagmann, L. Cammoun, X. Gigandet, R. Meuli, C. J. Honey, V. J. Wedeen, and O. Sporns, "Mapping the structural core of human cerebral cortex," *PLoS biology*, vol. 6, no. 7, p. e159, 2008.

[39] K. Javed, V. Reddy, and F. Lui, "Neuroanatomy, cerebral cortex," 2019.

[40] V. Fernández, C. Llinares-Benadero, and V. Borrell, "Cerebral cortex expansion and folding: what have we learned?" *The EMBO journal*, vol. 35, no. 10, pp. 1021–1044, 2016.

[41] P. Chavoshnejad, X. Li, S. Zhang, W. Dai, L. Vasung, T. Liu, T. Zhang, X. Wang, and M. J. Razavi, "Role of axonal fibers in the cortical folding patterns: A tale of variability and regularity," *Brain Multiphysics*, p. 100029, 2021.

[42] K. Zilles, E. Armstrong, A. Schleicher, and H.-J. Kretschmann, "The human pattern of gyrification in the cerebral cortex," *Anatomy and embryology*, vol. 179, no. 2, pp. 173–179, 1988.

[43] D. Dowsett, P. A. Kenny, and R. E. Johnston, *The physics of diagnostic imaging*. CRC Press, 2006.

[44] P. Armstrong and S. F. Keevil, "Magnetic resonance imaging: Basic principles of image production." *BMJ: British Medical Journal*, vol. 303, no. 6793, p. 35, 1991.

[45] R. W. Brown, Y.-C. N. Cheng, E. M. Haacke, M. R. Thompson, and R. Venkatesan, *Magnetic resonance imaging: physical principles and sequence design*. John Wiley & Sons, 2014.

[46] W. Nitz, "Principles of magnetic resonance imaging and magnetic resonance angiography," in *Clinical MR Imaging*. Springer, 2006, pp. 1–52.

[47] J. P. Lerch, A. J. van der Kouwe, A. Raznahan, T. Paus, H. Johansen-Berg, K. L. Miller, S. M. Smith, B. Fischl, and S. N. Sotiropoulos, "Studying neuroanatomy using mri," *Nature neuroscience*, vol. 20, no. 3, pp. 314–326, 2017.

[48] B. Fischl, "Freesurfer," *Neuroimage*, vol. 62, no. 2, pp. 774–781, 2012.

[49] Y. Mishchenko, "A fast algorithm for computation of discrete euclidean distance transform in three or more dimensions on vector processing architectures," *Signal, Image and Video Processing*, vol. 9, no. 1, pp. 19–27, 2015.

[50] J. E. Bresenham, "Algorithm for computer control of a digital plotter," *IBM Systems journal*, vol. 4, no. 1, pp. 25–30, 1965.

[51] P. S. Heckbert, "Digital line drawing," in *Graphics gems*. Academic Press Professional, Inc., 1990, pp. 99–100.

[52] C. Destrieux, B. Fischl, A. Dale, and E. Halgren, "Automatic parcellation of human cortical gyri and sulci using standard anatomical nomenclature," *Neuroimage*, vol. 53, no. 1, pp. 1–15, 2010.

[53] M. Lehtovirta, M. P. Laakso, G. B. Frisoni, and H. Soininen, "How does the apolipoprotein e genotype modulate the brain in aging and in alzheimer's disease? a review of neuroimaging studies," *Neurobiology of aging*, vol. 21, no. 2, pp. 293–300, 2000.

[54] C. DeCarli, "Part iv. neuroimaging in dementing disorders," *Disease-a-Month*, vol. 46, no. 10, pp. 707–724, 2000.

[55] G. Karas, E. Burton, S. Rombouts, R. Van Schijndel, J. O'Brien, P. Scheltens, I. McKeith, D. Williams, C. Ballard, and F. Barkhof, "A comprehensive study of gray matter loss in patients with alzheimer's disease using optimized voxel-based morphometry," *Neuroimage*, vol. 18, no. 4, pp. 895–907, 2003.

[56] I. B. Malone, D. Cash, G. R. Ridgway, D. G. MacManus, S. Ourselin, N. C. Fox, and J. M. Schott, "Miriad—public release of a multiple time point alzheimer's mr imaging dataset," *NeuroImage*, vol. 70, pp. 33–36, 2013.

[57] K. Im, J.-M. Lee, S. W. Seo, S. H. Kim, S. I. Kim, and D. L. Na, "Sulcal morphology changes and their relationship with cortical thickness and gyral white matter volume in mild cognitive impairment and alzheimer's disease," *Neuroimage*, vol. 43, no. 1, pp. 103–113, 2008.

[58] W. Lotmar, A. Freiburghaus, and D. Bracher, "Measurement of vessel tortuosity on fundus photographs," *Albrecht von Graefes Archiv für klinische und experimentelle Ophthalmologie*, vol. 211, no. 1, pp. 49–57, 1979.

[59] K. Chandrinos, M. Pilu, R. Fisher, and P. Trahanias, *Image processing techniques for the quantification of atherosclerotic changes*.   Department of Artificial Intelligence, University of Edinburgh, 1998.

[60] W. E. Hart, M. Goldbaum, B. Côté, P. Kube, and M. R. Nelson, "Measurement and classification of retinal vascular tortuosity," *International journal of medical informatics*, vol. 53, no. 2-3, pp. 239–252, 1999.

[61] K. G. Goh, W. Hsu, M. Li Lee, and H. Wang, "Adris: an automatic diabetic retinal image screening system," *Studies in Fuzziness and Soft Computing*, vol. 60, pp. 181–210, 2001.

[62] E. Grisan, M. Foracchia, and A. Ruggeri, "A novel method for the automatic grading of retinal vessel tortuosity," *IEEE transactions on medical imaging*, vol. 27, no. 3, pp. 310–319, 2008.

[63] M. Abdalla, A. Hunter, and B. Al-Diri, "Quantifying retinal blood vessels' tortuosity," in *2015 Science and Information Conference (SAI)*.   IEEE, 2015, pp. 687–693.

[64] L. J. Latecki and A. Rosenfeld, "Supportedness and tameness differentialless geometry of plane curves," *Pattern Recognition*, vol. 31, no. 5, pp. 607–622, 1998.

[65] R. C. James, *Mathematics dictionary Fourth edition*.   New York : Van Nostrand Reinhold Company Inc., 1976.

[66] L. A. Wulandhari and H. Haron, "The evolution and trend of chain code scheme," *Graphics, Vision and Image Processing*, vol. 8, no. 3, pp. 17–23, 2008.

[67] R. Klette and A. Rosenfeld, *Digital geometry: Geometric methods for digital picture analysis*.   Elsevier, 2004.

[68] T. Subba, A. Pradhan, and P. Rai, ""voxelization" in 3d searching-a study," *International Journal of Computer Applications*, 2015.

[69] R. Khilar, S. Chitrakala, and S. SelvamParvathy, "3d image reconstruction: Techniques, applications and challenges," in *2013 International Conference on Optical Imaging Sensor and Security (ICOSS)*, 2013, pp. 1–6.

[70] J. Seo, S. Chae, J. Shim, D. Kim, C. Cheong, and T.-D. Han, "Fast contour-tracing algorithm based on a pixel-following method for image sensors," *Sensors*, vol. 16, no. 3, p. 353, 2016.

[71] M. Ren, J. Yang, and H. Sun, "Tracing boundary contours in a binary image," *Image and vision computing*, vol. 20, no. 2, pp. 125–131, 2002.

[72] D. Coeurjolly, Y. Gerard, J.-P. Reveilles, and L. Tougne, "An elementary algorithm for digital arc segmentation," *Discrete Applied Mathematics*, vol. 139, no. 1-3, pp. 31–50, 2004.

[73] V. Kovalevsky, "New definition and fast recognition of digital straight segments and arcs," in *[1990] Proceedings. 10th International Conference on Pattern Recognition*, vol. 2.   IEEE, 1990, pp. 31–34.

[74] M. J. Mateos, A. Gastelum-Strozzi, F. A. Barrios, E. Bribiesca, S. Alcauter, and J. A. Marquez-Flores, "A novel voxel-based method to estimate cortical sulci width and its application to compare patients with alzheimer's disease to controls," *NeuroImage*, vol. 207, p. 116343, 2020.

[75] M. J. Mateos, J. Márquez, and E. Bribiesca, "3d tortuosity: a morphological characterization of the central sulcus to differentiate patients with alzheimer's disease and controls," in *2020 IEEE Nuclear Science Symposium and Medical Imaging Conference (NSS/MIC)*.   IEEE, pp. 1–4.

[76] S. Li, M. Xia, F. Pu, D. Li, Y. Fan, H. Niu, B. Pei, and Y. He, "Age-related changes in the surface morphology of the central sulcus," *Neuroimage*, vol. 58, no. 2, pp. 381–390, 2011.

[77] C. Peyrega and D. Jeulin, "Estimation of tortuosity and reconstruction of geodesic paths in 3d," *Image Analysis and Stereology*, vol. 32, no. 1, pp. 27–43, 2013.

[78] S. Pardo-Alonso, J. Vicente, E. Solórzano, M. Á. Rodriguez-Perez, and D. Lehmhus, "Geometrical tortuosity 3d calculations in infiltrated aluminium cellular materials," *Procedia Materials Science*, vol. 4, pp. 145–150, 2014.

[79] C. J. Gommes, A.-J. Bons, S. Blacher, J. H. Dunsmuir, and A. H. Tsou, "Practical methods for measuring the tortuosity of porous materials from binary or gray-tone tomographic reconstructions," *AIChE Journal*, vol. 55, no. 8, pp. 2000–2012, 2009.